

# We are IntechOpen, the world's leading publisher of Open Access books Built by scientists, for scientists

3,800

Open access books available

116,000

International authors and editors

120M

Downloads

Our authors are among the

154

Countries delivered to

TOP 1%

most cited scientists

12.2%

Contributors from top 500 universities



WEB OF SCIENCE™

Selection of our books indexed in the Book Citation Index  
in Web of Science™ Core Collection (BKCI)

Interested in publishing with us?  
Contact [book.department@intechopen.com](mailto:book.department@intechopen.com)

Numbers displayed above are based on latest data collected.  
For more information visit [www.intechopen.com](http://www.intechopen.com)



# Graphene-Based Nanocomposites

Xin Wang and Sheng Chen

*Key Laboratory for Soft Chemistry and Functional Materials,  
Nanjing University of Science and Technology, Ministry of Education,  
China*

## 1. Introduction

Since the historical observation of single layer graphene by Geim and his co-workers in 2004, this atomically thin carbon film has received ever-increasing attention and become a rapidly rising star on the horizon of materials science and condensed-matter physics (Novoselov et al., 2004). Graphene exhibits many unusual and useful properties such as a large theoretical specific surface area ( $2630 \text{ m}^2 \text{ g}^{-1}$ ) (Stoller et al., 2008), high values of Young's modulus ( $\sim 1.1 \text{ Tpa}$ ), excellent thermal conductivity ( $\sim 5000 \text{ W m}^{-1} \text{ s}^{-1}$ ) (Park & Ruoff, 2009), and amazing intrinsic mobility ( $200\,000 \text{ cm}^2 \text{ v}^{-1} \text{ s}^{-1}$ ). Moreover, the extraordinary transport phenomena of graphene have also been well documented, including massless Dirac fermions (Novoselov et al., 2005), ambipolar field effect (Novoselov et al., 2004), room-temperature quantum Hall effect (Zhang et al., 2005), etc. These fascinating performances have attracted extensive concern in recent years with ever-increasing scientific and technological impetus. Among the numerous methods for harnessing these peculiar properties, one possible route would be to incorporate graphene sheets into composite materials (Stankovich et al., 2006). The easy synthesis, low cost and non-toxicity of graphene make this material a promising candidate for many technological applications (Geim & Novoselov, 2007; Allen et al., 2010). For example, graphene sheets are excellent nanoscale substrates for the formation of silver-nanoparticle films. These silver-nanoparticle films assembled on the single-layer sheets are flexible and can form stable suspensions in aqueous solutions (Xu et al., 2009). They can be processed facilely into paper-like materials and flexible electronic materials to satisfy different requirements for many products, such as membranes, anisotropic conductors, biological sensors and optoelectronic nano-devices, etc. Graphene sheets and exfoliated graphene oxide possess large surface areas and thus may be excellent support materials to disperse and stabilize inorganic nanoparticles, such as Pt,  $\text{Co}_3\text{O}_4$ , CuO,  $\text{MnO}_2$ ,  $\text{MnOOH}$ ,  $\text{Co}(\text{OH})_2$ , etc., effectively inhibiting the aggregation in post-synthesis and thereby giving a relatively higher utilization of the active material. Decoration of graphene sheets with nanoparticles has been demonstrated to reveal special features in new hybrids that can be widely utilized in catalysts, supercapacitors, Li-ion batteries, etc. It was found that the introduction of less amount of graphene oxide into PANI could induce a synergistic effect, greatly enhancing the electrochemical performance of PANI as a supercapacitor electrode material (Wang et al., 2009a).

The intent of this chapter is to provide a basic overview of graphene-based nanocomposites. The emphasis is primarily on the different synthetic strategies that have been pursued so far

for the preparation of graphene supported inorganic nanoparticles and graphene-doped polymers, as well as the concerted effect of the properties of the individual components in the new hybrid materials that will present special features for catalysts, electrochemical materials and nanotechnology. Additionally, the prospective applications of these graphene-based materials will also be presented.

## 2. Graphene-based nanocomposites

### 2.1 A general method for preparing graphene-based nanocomposites

As a basic building block for graphitic materials of all other dimensionalities (Geim & Novoselov, 2007), graphene has suffered from a problem that was in the early days of nanotube and fullerene research. A prerequisite for exploiting most proposed applications for graphene is the availability of processable graphene sheets in large quantities. Until recently, two main routes are fully exploited: large-scale growth and large-scale exfoliation. Some techniques, such as liquid-phase exfoliation of graphite (Hernandez et al., 2008; Lotya et al., 2009), chemical vapour deposition (Lo'pez et al., 2010; Park et al., 2010), helium arc-discharge (Wu et al., 2010), large growth or self-assembly approach (Weixia et al., 2009; Li et al., 2009) and chemical reduction of GO (Li et al., 2008; Williams et al., 2008), have taken us a step closer to real-world applications of this intriguing material.

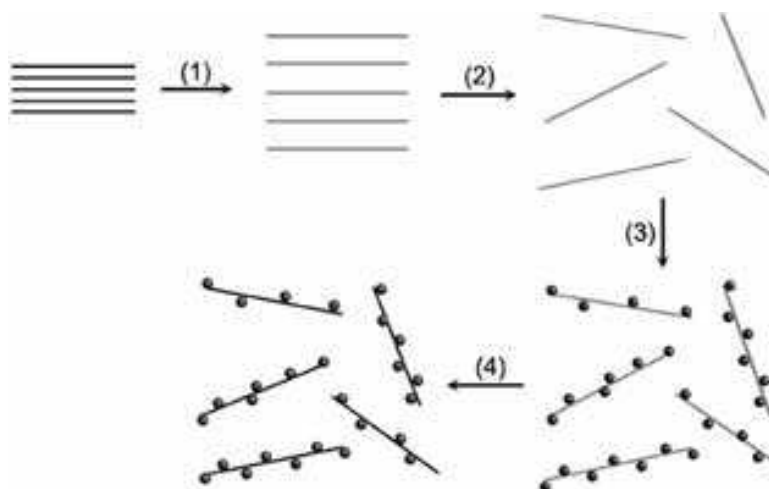


Fig. 1. A schematic route for anchoring nanoparticles onto graphene sheets. (1) Oxidation of graphite (black lines) to GO (gray lines) with greater interlayer distance. (2) Exfoliation of GO to graphene oxide sheets by sonication in water solution. (3) Attachment of metal particles on the graphene oxide sheets. (4) Formation of graphene-supported metal particles composites by reduction of the graphene oxide sheets. The distorted carbon sheets are simplified to an idealized planar model (Xu et al., 2008a).

Among above-mentioned strategies for manufacturing graphene-based nanocomposites, which requires not only that graphene sheets be made on a large scale but that they should be homogeneously distributed, chemical reduction of GO seems to be a much more efficient, low-cost, and bulk production pathway to incorporate graphene sheets into hybrids. As shown in Figure 1, the current main interests in preparing graphene-based nanocomposites are concentrated on exfoliating graphene through a combination of oxidation and sonication procedures, followed by reduction through chemical methods (Xu et al., 2008a). The GO is heavily oxygenated graphene bearing carbonyl, hydroxyl, and

epoxy groups on the basal planes as well as carboxylic groups on the edges of the carbon sheets (Boukhvalov & Katsnelson, 2008). The functional groups on GO can serve as anchor sites and consequently make the in situ formed nanoparticles attach on the surfaces and edges of GO sheets. It should be mentioned that GO is gradually lost its excellent electrical properties and eventually becomes electrically insulated owing to the transformation of carbon atoms from a planar  $sp^2$ -hybridized geometry to a distorted  $sp^3$ -hybridized geometry (Stankovich et al., 2006). To recover electrical conductivity, eliminating most of the oxygen-containing functional groups of GO to restore the aromatic graphene networks is necessary.

## 2.2 Flexible metal-nanoparticle films

Flexible paper-shaped materials are of great importance in our technological society. Their typical utilizations include chemical filters, adhesive layers, molecular storage, and batteries and supercapacitors films (Dikin et al., 2007). In the past several years, metal nanoparticles, in particular noble metal nanoparticles (e.g., Au and Ag) have generated extensive interest due to their unique electronic, optical, and catalytic properties. Alignment of metal nanoparticles into thin films is of great importance for diversified applications. The substrate is a necessary to prepare nanoparticle films, for example, metal foils, glass plate, polymer films, silicon wafers, and so on have been widely used as substrates for nanoparticle assembling. Unfortunately, most of these substrates are bulk materials with rigid morphology, making the post-processing of as-synthesized nanoparticle films remain an insurmountable challenge. It is desirable to explore a flexible nanoscale substrate for assembling nanoparticles, thereby forming the flexible nanoparticle films.

Graphene sheets are attractive recently as excellent nanoscale building blocks for producing new composites. GO is heavily oxygenated graphene that is readily exfoliated in water to yield stable dispersions consisting mostly of single-layer sheets. In view of the pliable nature of graphene and GO, the preparation of graphene oxide paper and graphene sheets films have been reported, which have shown a combination of both macroscopic flexibility and stiffness, and has found use in many fields (Dikin et al., 2007; Li et al., 2008). Commonly, the silver mirror reaction has been used as an efficient method for preparing silver nanoparticles films using GO as substrates (Xu & Wang, 2009). It is known that silver-nanoparticle films are easily coated on bulk substrates by simply dipping these substrates in the reaction solutions. Because the hydrophilic GO can be exfoliated in water to form stable single-layer sheets, which can be regarded as immersed substrates, accordingly, it is possible that silver-nanoparticle films may form on the nanoscale 2D carbon sheets when dipping these exfoliated GO sheets, instead of bulk substrates, in the reaction solution. Therefore, an idea of using graphene oxide sheets as the nanoscale substrates for the formation of silver-nanoparticle films is examined.

Fig. 2 displays the typical TEM and FESEM images of silver nanoparticles on graphene oxide sheets. In Fig. 2a, the almost transparent 2D carbon sheets were thickly decorated by the silver particles. The monolayer carbon nanosheets were so thin that it was difficult to distinguish them with the carbon-supported films on the copper grid. However, the edges and crumpled silk waves of these carbon sheets lead us to believe that these nanoparticles are indeed deposited on supports. Moreover, as shown in Figure 2c and d, it can be clearly observed that these as-synthesized silver nanoparticle films can restack and large amounts of silver nanoparticles assembled on the 2D substrates. Commonly, the graphene oxide bears functional groups on the basal planes and edges. These negative charged functional

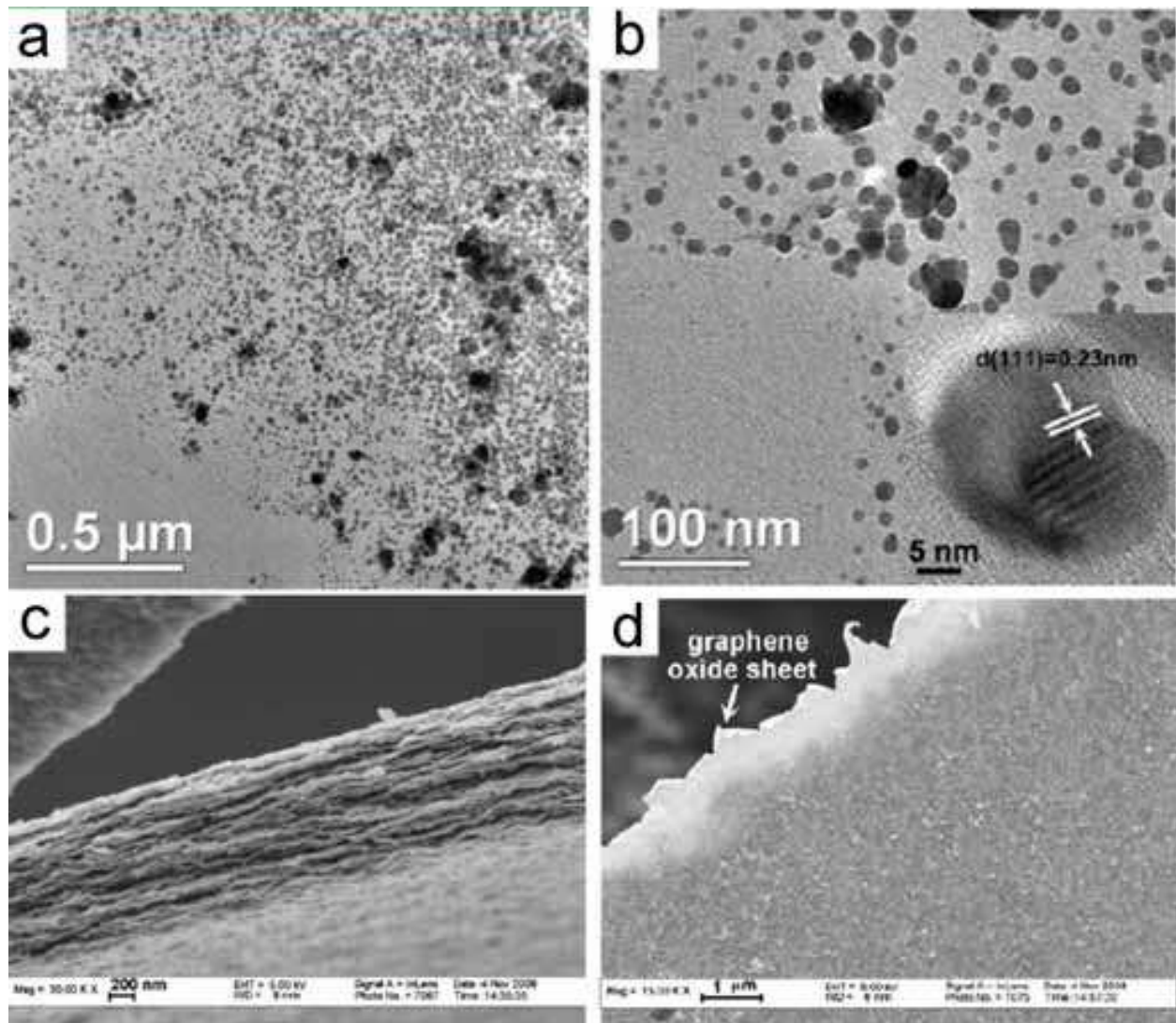


Fig. 2. TEM (a, b) and FESEM (c, d) images of silver nanoparticles on graphene oxide sheets (Xu & Wang, 2009).

groups can be used as anchors to adsorb polar materials and inorganic nanoparticles. Accordingly,  $\text{Ag}(\text{NH}_3)_2^+$ , as a positive ion, can easily interact with these negative graphene sheets through electrostatic forces. The in situ reduction of these ions by glucose allows these silver nanoparticles to anchor onto the graphene oxide sheets, and some anchored onto the edges.

It has been well documented that the stable graphene-based sheets aqueous solution can be readily processed into films and paper-like materials (Stankovich et al., 2006; Li et al., 2008). When drying on a substrate, the silver-coated graphene oxide sheets have also easily assembled to form a macroscopic film with a shiny metallic luster that exhibited mirror-like properties (Figure 3). Nevertheless, the film consisting of individual graphene oxide sheets was dim and possessed poor reflectivity. It is believed that the silver-mirror films are usually originating from the assembly of silver nanoparticles on bulk substrates. In this system, the macroscopic mirror-like films obtained can be attributable to the restacking of silver nanoparticle films (Fig. 2c).

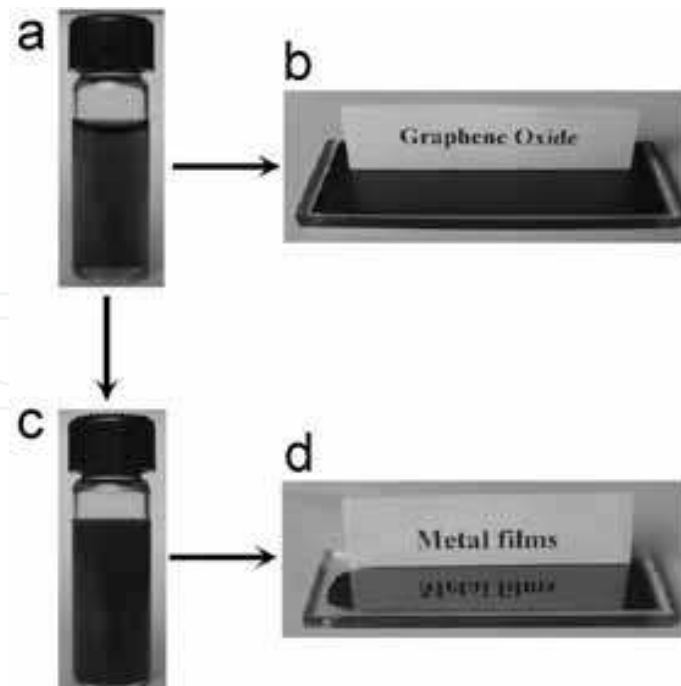


Fig. 3. Photos of graphene oxide and Ag-GO composite in water solution and dried. (a) A vial containing a suspension ( $0.25 \text{ mg mL}^{-1}$ ) of graphene oxide in water; (b) the graphene oxide film obtained by drying 60 mL of the dispersion on glass; (c) after coating by silver nanoparticles, the Ag-GO composite can form a stable suspension in a water solution with  $0.25 \text{ mg mL}^{-1}$  of graphene oxide; (d) The mirror-like film obtained by drying the suspensions of composite on glass (Xu & Wang, 2009).

Traditionally, the substrates for particle films are bulk materials. Free-standing films without any supports have also been prepared, but further processing of these films meets difficulties. Therefore, the nanoscopic substrates with flexible properties are beneficial for the use of particle films in practical technologies. The idea of using pliable graphene oxide sheets as substrates to prepare nanoparticle films can also be extended to other materials, such as metal and semiconductor particles. These flexible and adjustable nanoparticle films may show promising application in optics, sensors, catalysis, etc., broadening the horizon for the vast use of particle films.

### 2.3 Catalysis

Catalysis, an integral part in our daily life, has extensively utilized in a variety of technological fields. Recent studies continuously concentrate on the preparation and applications of nanoscale particles of metal or metal oxides, owing to their large specific surface area and high activity in most catalytic processes. Ammonium perchlorate (AP) is one of the main oxidizing agents that is widely used in various propellants (Boldyrev, 2006). The burning behaviour of propellants is highly relevant to the thermal decomposition of AP. Development of novel catalysts with high decomposition efficiency to produce large amount of energy as far as possible and to decrease the burning temperature for easy operation and control is of great significance for its practical applications. Generally, the thermal decomposition of AP takes place in three steps: the endothermic phase transition at around  $240 \text{ }^{\circ}\text{C}$ , the low-temperature decomposition at around  $316 \text{ }^{\circ}\text{C}$  (LTD) and the high-temperature decomposition at around  $460 \text{ }^{\circ}\text{C}$  (HTD). To increase the exothermic heat and bring down the temperatures of decomposition are very important. It is demonstrated that metal oxide and hydroxide nanoparticles, like

$\text{Co}_3\text{O}_4$ ,  $\text{CuO}$ , and  $\text{MnOOH}$ , could promote the heterogeneous decomposition of deprotonized  $\text{HClO}_4$  gas on the solid surface in the high-temperature decomposition, which will reduce the HTD and increase exothermic quantity in the decomposition process. However, in the post-synthesis of these materials, aggregation occurs when they were dried in air, resulting in a decrement of the catalytic capability. Considering the large specific area of graphene sheets or GO, which is desirable to disperse and stabilize the inorganic nanoparticle, the combination of graphene or GO with nanoparticles may effectively inhibit the aggregation and consequently give a higher catalytic performance.

Fig. 4 shows the TEM, FESEM, and DSC characterization of as-prepared  $\text{GO-Co}_3\text{O}_4$  nanocomposites (Xu et al., 2008b). From Fig. 4a-c, it is clearly seen that the exfoliated GO sheet was decorated randomly by uniform spherical particles of about 100 nm in size. These in situ formed particles could result in exfoliating the layered GO. In Fig. 4c of the dark field TEM images of  $\text{GO-Co}_3\text{O}_4$  nanocomposites, it is interesting that some of the  $\text{Co}_3\text{O}_4$  nanoparticles are brighter than the ones which seem to be enveloped by a thin film. This may be attributed to the fact that the functional groups, especially hydroxyl and epoxy groups appear on both sides of the graphene oxide sheet, and thereby in situ formed  $\text{Co}_3\text{O}_4$  could anchor on both sides of the supports.

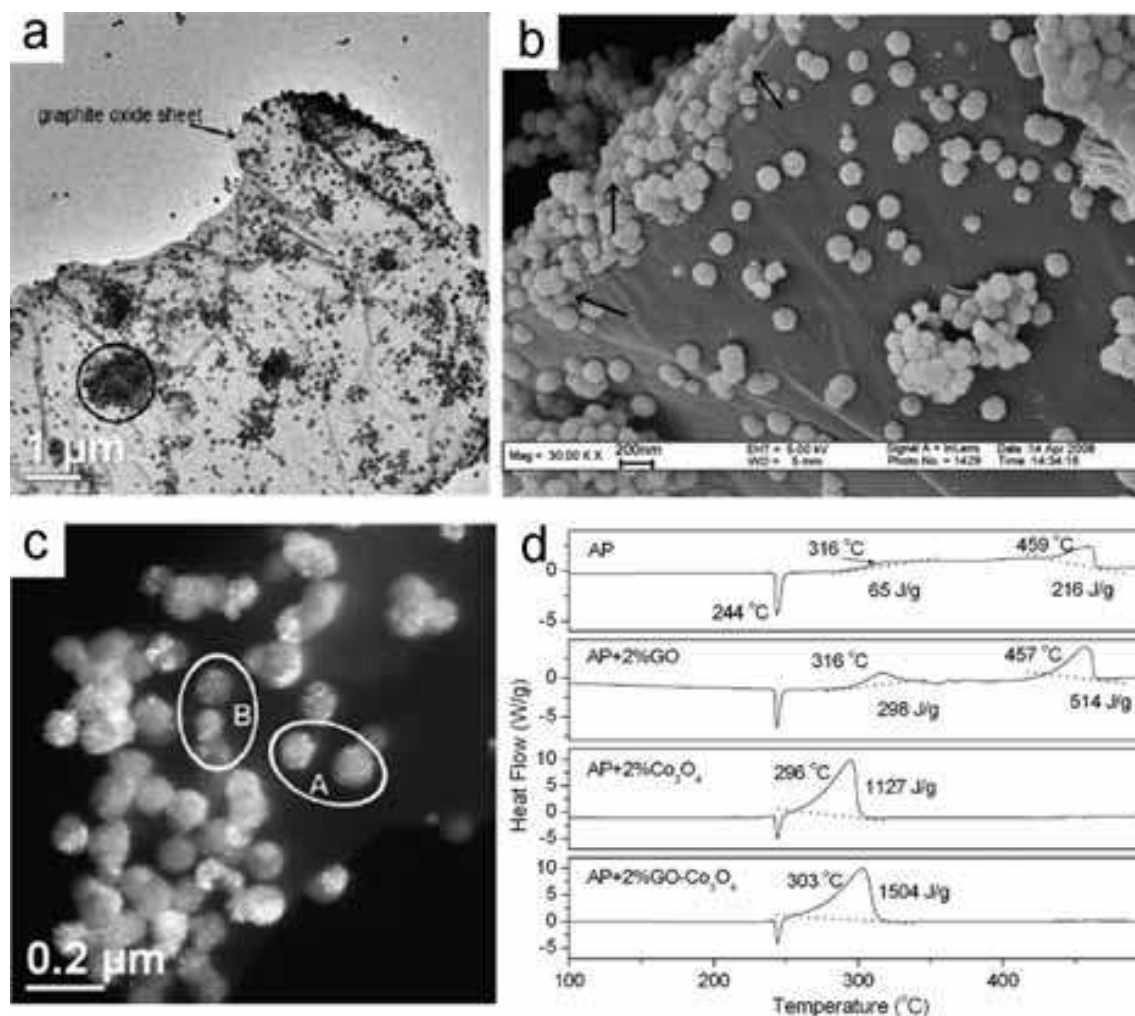


Fig. 4. TEM (a, c), FESEM (b) images of  $\text{GO-Co}_3\text{O}_4$  nanocomposites; (d) DSC curves for the decomposition of AP, AP with 2% GO, AP with 2%  $\text{Co}_3\text{O}_4$  and AP with 2%  $\text{Co}_3\text{O}_4$ -GO nanocomposite (Xu et al., 2008b).

To explore the catalytic effect of this nanocomposite on thermal decomposition of AP, DSC measurement is conducted. Figure 4d displays that when individual GO was added, two exothermic peaks of AP became apparent, along with a new exothermic peak centred at around 360 °C, and the exothermic heat of the two steps was larger than that of AP. This may be due to the catalytic effect of GO in the system. The introduction of  $\text{Co}_3\text{O}_4$  and GO- $\text{Co}_3\text{O}_4$  reduced temperature of both LTD and HTD and made the two steps blend almost into one process. The decomposition temperature of AP with 2%  $\text{Co}_3\text{O}_4$  (296 °C) was close to that of AP with 2% GO- $\text{Co}_3\text{O}_4$  (303 °C); however, the former exothermic quantity (1127 J/g) was much lower than that of the latter (1504 J/g). Therefore, owing to the concerted effect of the individual components for the catalysis of decomposition of AP, the addition of GO- $\text{Co}_3\text{O}_4$  not only brought down the decomposition temperature, but also increased the exothermic heat of AP, exhibiting good catalytic properties.

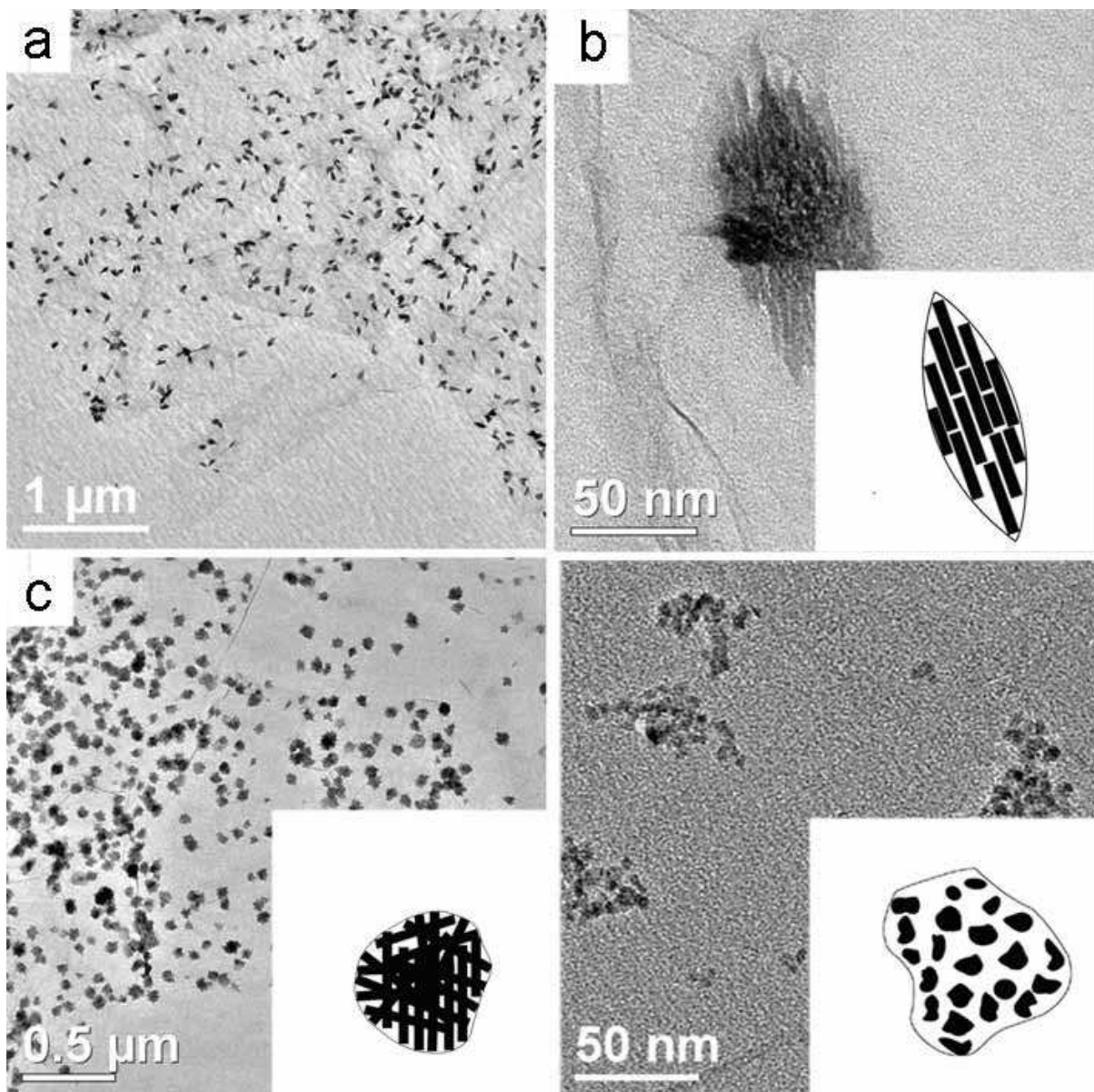


Fig. 5. TEM images of GO decorated CuO nanoparticles with different morphologies. (a-b) spindle-like CuO; (c) spherical CuO; (d) CuO nano-aggregates (Zhu et al., 2010).

Moreover, the composite of GO support CuO nanoparticles has been synthesized for the first time (Zhu et al., 2010). It should be mentioned that we can tune the catalytic performances by shape-controlled synthesis of different morphological nanoparticles on GO sheets. As displayed in Fig. 5, by varying the volume ratios of the added water and isopropanol and mass ratios of CuO/GO, the composite of CuO nanoparticles with different morphologies, including spindles, spheres, and nano-aggregates, on exfoliated GO sheets have been dramatically obtained. DSC tests display discrepant catalytic effects of these composites on AP. The HTD and exothermic quantity of AP mixed with 2% spindle-like CuO-GO, spherical CuO-GO, and CuO nano-aggregates-GO are 330 °C (1056 J g<sup>-1</sup>), 315 °C (1347 J g<sup>-1</sup>) and 321 °C (1297 J g<sup>-1</sup>), respectively. The spherical CuO nanocrystals on GO sheets have shown the best catalytic action. In addition, the introduction of pure CuO and the composite of spherical CuO nanocrystals on GO sheets could both decrease the temperatures. However, the HTD and exothermic quantity of AP mixed with 2% spherical CuO-GO composites (315 °C, 1347 J g<sup>-1</sup>) was much competitive than that of pure CuO (334 °C, 1093 J g<sup>-1</sup>), suggesting the catalytic properties of the nanocomposites are enhanced by the concerted effect between GO and CuO.

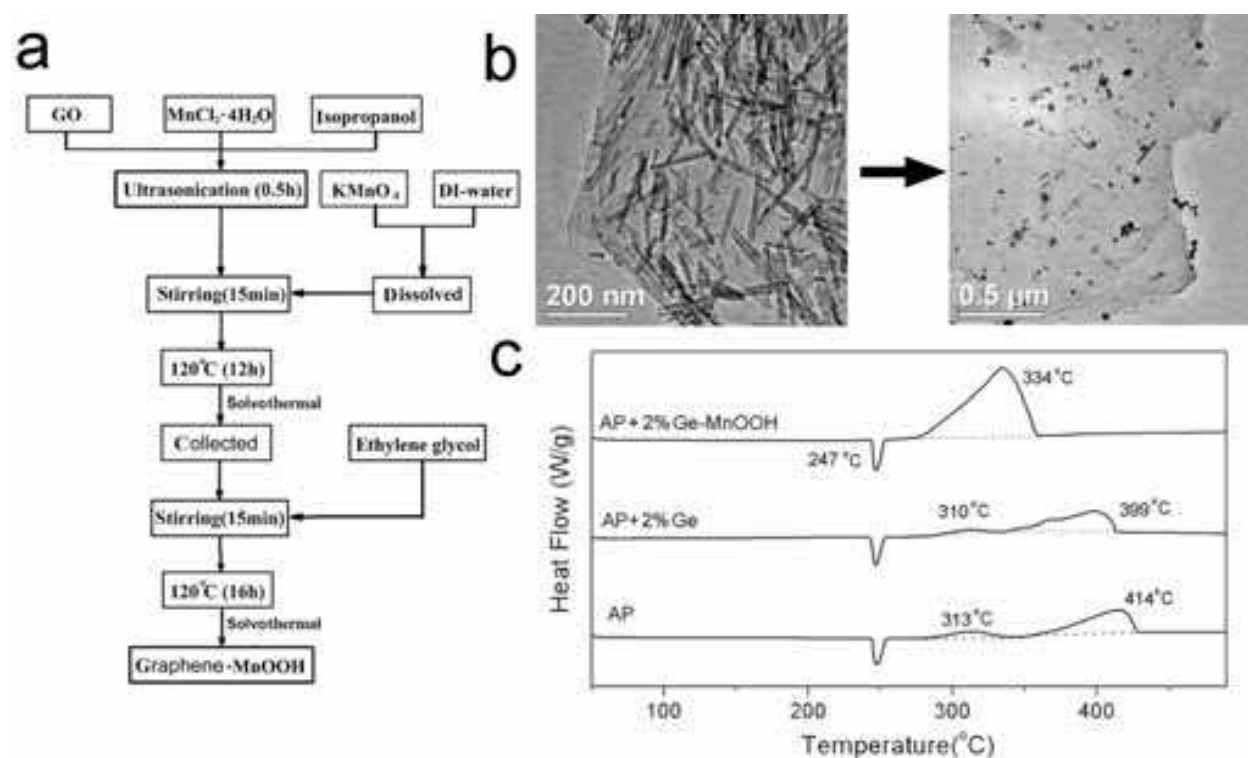


Fig. 6. (a) Preparation procedure of graphene-MnOOH nanocomposites; (b) TEM images of GO-MnO<sub>2</sub> and graphene-MnOOH nanocomposites; (c) DSC curves for the thermal decomposition of AP, AP with 2% graphene, and AP with 2% graphene-MnOOH nanocomposites (Chen et al., 2010a).

Generally, GO is insulated owing to the introduction of large amounts of functional groups, eliminating most of the oxygen-containing functional groups of GO to restore the aromatic graphene networks is necessary for obtaining graphene sheets. In Figure 6a, a two-step solvothermal procedure was developed to synthesize graphene-MnOOH nanocomposites through reducing GO-MnO<sub>2</sub> using ethylene glycol (Chen et al., 2010a). Initially, GO sheets

were decorated randomly by the rod-like  $\text{MnO}_2$  (the left image in Figure 6b), where a significant morphological transformation is observed after solvothermal treatment with ethylene glycol. The rod-like  $\text{MnO}_2$  transfers to particulate  $\text{MnOOH}$  with diameters ranging from 20 to 80 nm. The dissolution-crystallization mechanism is speculated to be responsible for this process. Additionally, the catalysis of as-obtained graphene- $\text{MnOOH}$  nanocomposite on the decomposition of AP was displayed in Fig. 6c. With the addition of 2% graphene into the system, the LTD and HTD decreased to 310 and 399 °C, respectively, probably due to the catalytic action of graphene. However, when graphene- $\text{MnOOH}$  nanocomposites were added, the two steps (LTD and HTD) blended into one process at 334 °C with the exothermic heat (1392 J g<sup>-1</sup>) much larger than that of net AP and AP-graphene composites (590 and 540 J g<sup>-1</sup>), revealing a good catalytic effect. Although in the actual process the decomposition of AP would involve many additional steps, the results of graphene (GO)- $\text{MnOOH}$  ( $\text{Co}_3\text{O}_4$ ,  $\text{CuO}$ ) calculated from the DSC measurements are still believed of great significance for material investigation.

#### 2.4 Surface-enhanced Raman scattering

Raman spectroscopy is a powerful technique that is nondestructive, fast, and could provide detailed information as to molecular structures. However, recent Raman researches are limited by its low sensitivity. Raman scattering (SERS) is able to overcome this obstacle and provide a spectral intensity often enhanced by many orders of magnitude for molecules adsorbed on a properly fabricated metal (e.g., Ag, Au, and Pt) surface. This offers the opportunities for SERS to facilitate the study of structural and electronic information of molecules with high resolution (Ferrari, 2007).

It is generally accepted that two mechanisms are contributable to the SERS: the electromagnetic and the charge transfer mechanisms (Fu et al., 2010a). Another enhancement can also be acquired from molecular resonances, but they are only considered in specific system. The electromagnetic enhancement usually can contribute factors of about  $10^4$ - $10^6$  to the Raman enhancement. While the charge transfer enhancement involves the chemisorption interaction and the metal-adsorbate charge transfer, and is usually said to contribute factors of about 10-100 of the observed enhancement.

The typical features for graphene or GO in Raman spectra are the D band around 1360 cm<sup>-1</sup> and the G band around 1600 cm<sup>-1</sup>, corresponding to the breathing mode of  $\kappa$ -point phonons of  $A_{1g}$  symmetry and the first-order scattering of the  $E_{2g}$  phonons, respectively. Absorption of noble metallic-nanoparticles, like Ag, Au, and Pt, onto graphene or GO sheets is a feasible way to study of graphene sheets in detail. As mentioned in chapter 3.2, silver nanoparticles can form flexible film on GO sheets. On the contrary, we can also regard these one-atom-thick 2D nanostructures as monolayer molecules adsorbed on silver-nanoparticle films (Xu & Wang, 2009). The energy-dispersive X-ray spectrometry (EDS) analysis in Figure 7d indicated that the surface of the film was almost completely covered by elemental silver, which consequently enabled such macroscopic films to display a metallic luster (Figure 7c). Therefore, the as-synthesized silver-nanoparticle films in this system may also display SERS activity. It is obvious in Fig. 7a that the intensities of the D and G bands of GO are enhanced in comparison with those of the original GO. The level of enhancement factor of the Raman scattering is calculated to be about one order of magnitude. Thus, the SERS in this sample may originate from the chemical effect. Additionally, the degree of enhancement of Raman spectra in the system can be controlled by adjusting the quantity of silver particles. As shown in Fig. 7b, the intensities of D and G bands increase along with the incremental

density of the coating silver particles and gradually become stable. This phenomenon may be explained by the fact that the number densities of the anchor sites between the GO and silver nanoparticles are constant. Consequently, when saturation of the charge-transfer complexes is reached, further elevated quality of silver may have little influence on the intensities of the D and G bands.

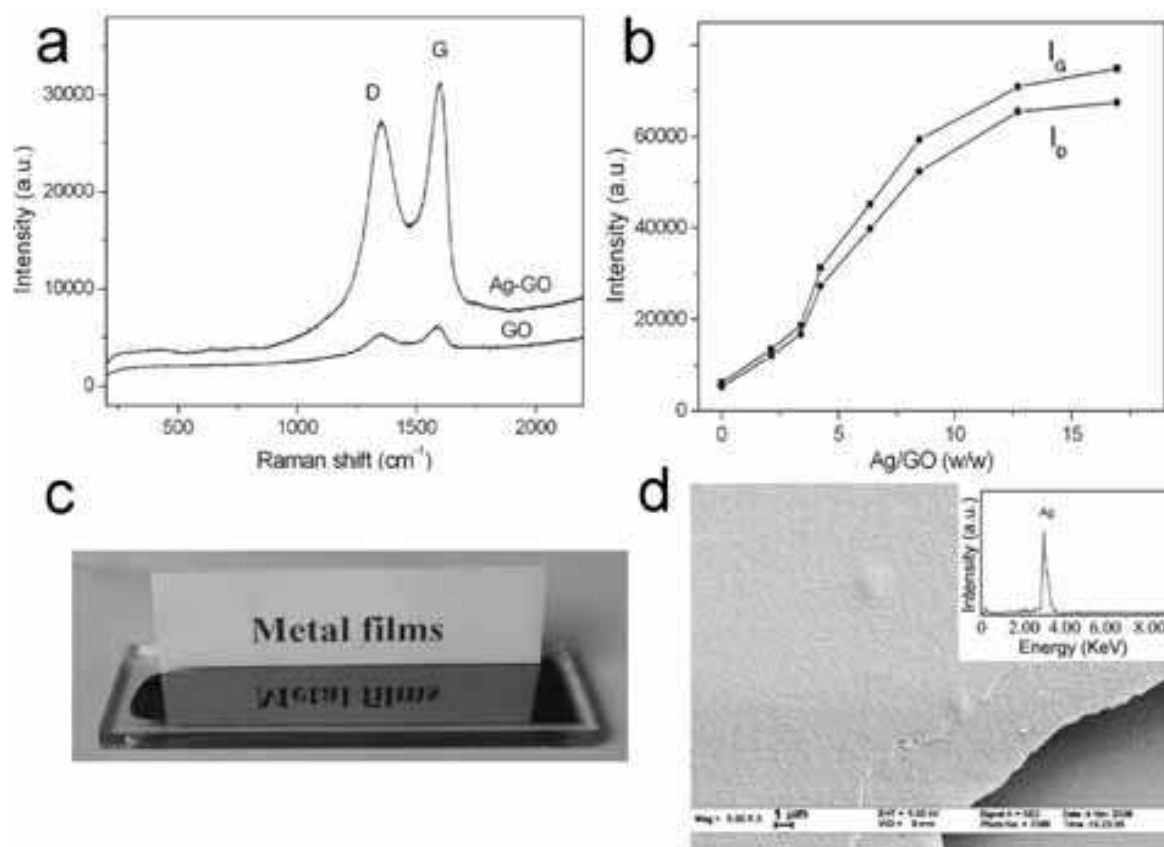


Fig. 7. (a) Raman spectra of GO and SERS spectra of Ag-GO composites with 80 wt% Ag; (b) The relationships between the intensity of the D and G bands of GO and the quality of silver in the composites; (c) the mirror-like film obtained by drying Ag-GO suspensions on glass; (d) FESEM images and EDS spectrum of the Ag-GO hybrid films (Xu & Wang, 2009).

To better understand the energy transfer mechanisms in graphene-based composites, which can provide a template for creating novel nanostructured derivatives, the graphene-Au sheets were fabricated (Xu & Wang, 2009). The composite was then removed to the surface of Si wafer pre-cleaned with ethanol and water to give high quality SERS spectra. By varying the excitation wavelength of lasers, the SERS excitation profile of graphene-Au was acquired.

The morphologies of the graphene-Au nanocomposites was obtained using TEM and SEM as shown in Fig. 7a and b. It is clearly seen that most metal nanoparticles distribute randomly on the supports. Despite there are some large triangular gold particles on the sheets, most are nano-spheres. In Fig. 7b, the sheets become more corrugated after the attachment of gold nanoparticles. The upper inset EDS images show that graphene-Au contain mainly the element Au, apart from the initial C and O. Additionally, the ratio of the contents (O/C) is lower compared to that of GO, suggesting the deoxygenation of GO to form graphene.

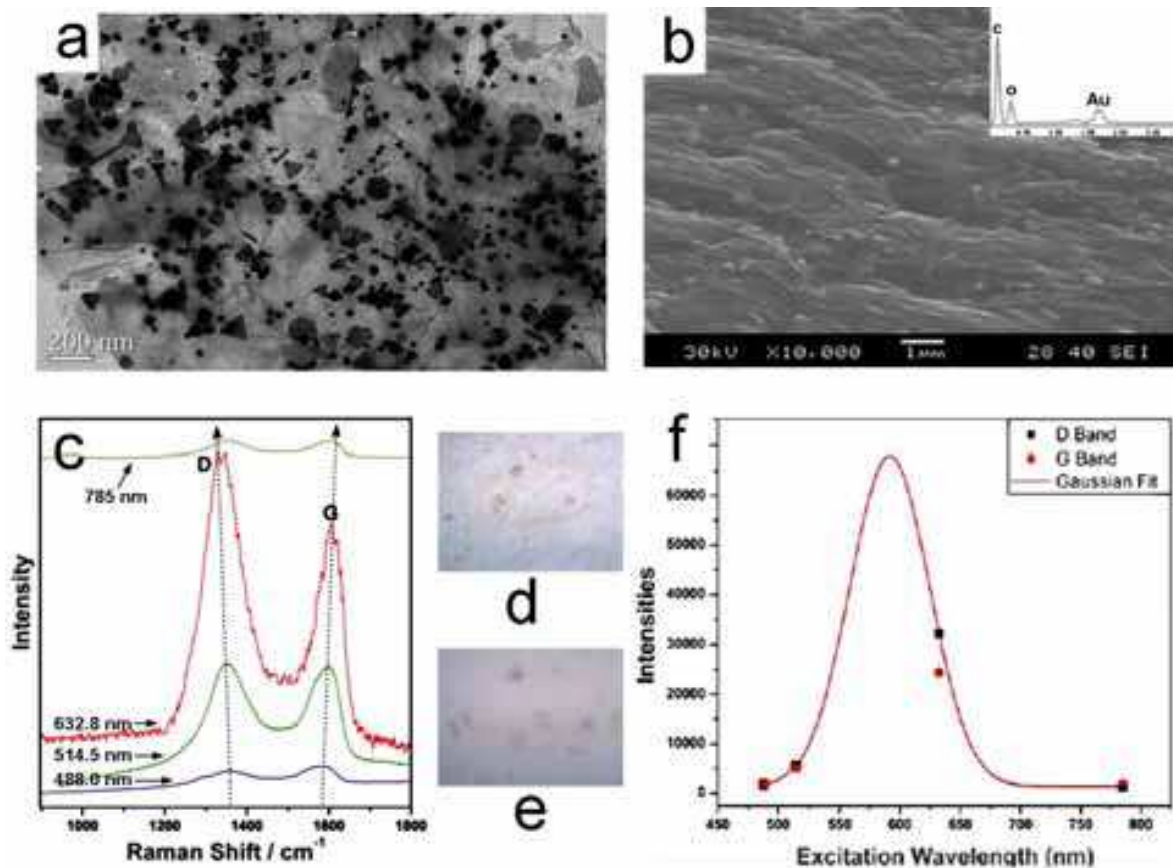


Fig. 8. (a) TEM (b) SEM images of graphene-Au nanocomposites; the inset of (b) is EDS images; (c) Raman spectra of G-Au at excitation wavelengths of 785, 632.8, 514.5, 488 nm; (d) G-Au (e) GO on the Si wafer that were observed under Raman microscopy and taken for the Raman measurements; (f) excitation profile of the D and G bands of graphene enhanced with Au nanoparticles (Fu et al., 2010a).

Raman spectra of graphene-Au at different excitation wavelengths are shown in Fig. 8c. To the right of the Raman spectra, Figure 8d and 8e show the images of graphene-Au and GO on the Si wafer that were observed under Raman microscopy and taken for the Raman measurements. The sheets of G-Au and GO seem to be one or two layers on Si wafer, and the sheets are smaller after decorated with Au nanoparticles. Similar to the Raman spectrum of pure GO (Fig. 6a), the G-Au Raman line at 488 nm, also contains both D and G bands however, with an increased D/G intensity ratio. Specifically, the peak intensity ratio ( $I_D/I_G$ ) decreases from approximately 1.0 for GO to about 0.75 for the reduced sample. This observation makes sense regarding to the formation of more extended networks of conjugated  $sp^2$  carbons, towards a more locally ordered graphene lattice.

In addition, Fig. 8c displays that at different wavelengths, the intensity of the D band was enhanced  $\sim 5$  times when we measured with 514.5 nm excitation wavelength compared to that of GO, and  $\sim 27$  times for 632.8 nm excitation wavelength. For the G band, enhanced factor is 3 for 514.5 nm and 16 for 632.8 nm excitation, respectively, in comparison with that of GO. However, the intensity decreased considerably in the case of excitation wavelength changed to 785 nm. In Fig. 8d, we provide an excitation profile of the D and G bands. Note that this profile indicates a resonance. A Gaussian fit to the D band profile gives a maximum of 2.09 eV (593 nm) and a width of 0.30 eV.

Commonly, the plasmon resonance of Au is  $\sim 548$  nm, at some distance from the excitation profile maximum of about 593 nm. Aggregation of gold nanoparticles can lead to a red shift of the plasmon resonance. Although the TEM images show a significant fraction of larger nanoparticles, seldom shift was observed in the absorption spectrum, nor any other significant maximum besides that at 548 nm, even at higher concentrations. It is common in SERS to observe a difference between the plasmon resonance and the maximum of the excitation profile. The discrepancy was mainly due to contributions from charge transfer transitions between the molecule and metal. It should be mentioned that the work function of Au is  $-5.3$  eV (relative to the vacuum level) and that of graphite (presumably close to that of the nanotubes) is  $-4.5$  eV, therefore, a charge transfer from the graphite to the metal is expected to occur with ease at a Raman excitation wavelengths of 514.0 nm, resulting in the Fermi level shift.

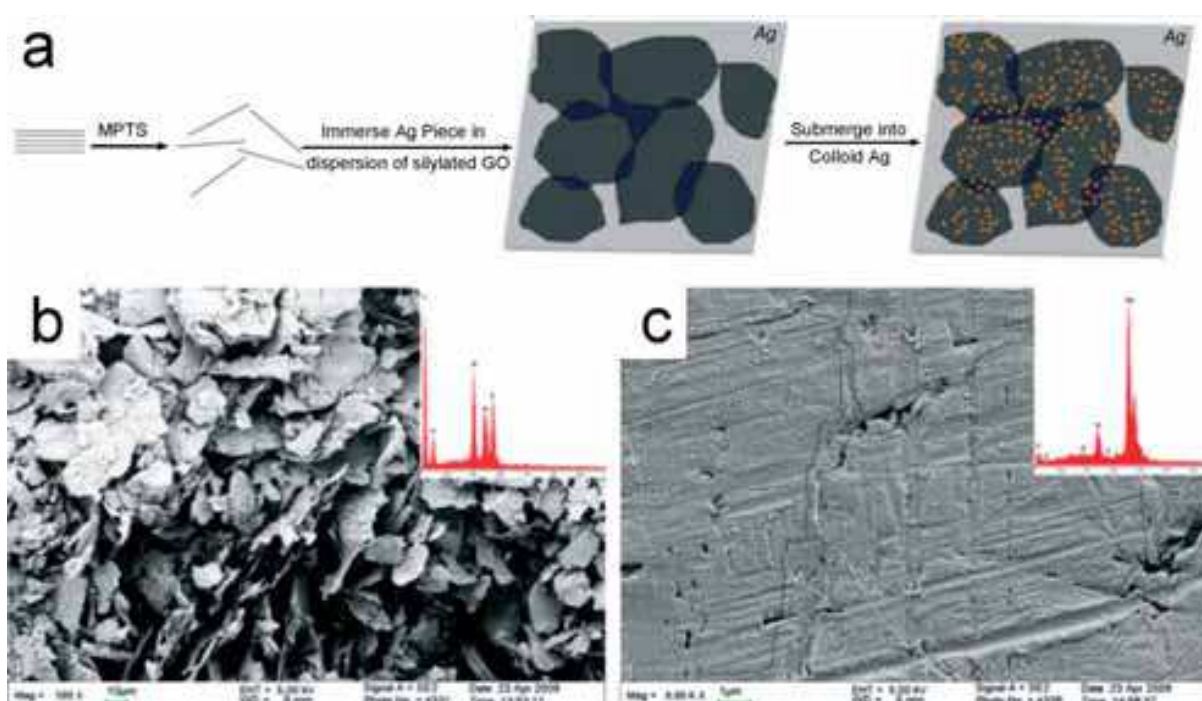


Fig. 9. (a) Scheme showing a proposed formation processes of Ag piece/GO/colloidal Ag sandwiches. SEM images of (b) MPTS-GO and (c) Ag piece/GO/colloidal Ag sandwiches. The inset shows the EDS image (Fu et al., 2010b).

To get a large enhancement, a structure of Ag piece/GO/colloidal Ag sandwiches is devised (Fu et al., 2010b). The typical route involves self-assembly of silylated GO sheets on a silver piece and then submerges the piece into colloidal Ag (Fig. 9a). It is seen from TEM, SEM and EDX analyses that the lamellar structures of GO sheets and the size of Ag particles remained, although the GO layers were exfoliated and destroyed after silylation (Fig. 9b and c). Remarkably, the enhanced factor of GO in this system is estimated to be about  $10^4$ . The large enhancement of the SERS spectrum of silylated GO sheets can be attributed to the electromagnetic coupling of the colloidal Ag nanoparticles and the surface of the Ag piece, most probably due to the interactions of the localized surface plasmon of colloidal Ag nanoparticles and the surface plasmon polariton of the Ag piece. This research extends the capability of SERS investigations to GO products and points to a promising future for the fabrication of thin films with smart properties.

## 2.5 Methanol fuel cells

In recent years, fuel cells have been extensively considered as very promising devices, which convert the chemical energy of a fuel (hydrogen, natural gas, methanol, gasoline, etc.) and an oxidant (air or oxygen) into electricity. Among them, the direct methanol fuel cell (DMFC) has been developed for portable devices, such as mobile phones and laptops owing to its simple design and operation. The direct oxidation of methanol is a key step during DMFC operation and has been extensively investigated. Platinum is taken as the most active metal for methanol oxidation. However, individual Pt particles for methanol adsorption has subjected to low DMFC power density, low CO toleration, and short cycle life. Therefore, on one hand, Pt-based multiple alloys have been explored, for example the binary Pt-Ru alloy is generally accepted as the most promising candidate for improving DMFC performance. On the other hand, to improve deposition of Pt alloys nanoparticles onto carbon supports are demonstrated as an effective pathway. Given the cost-effectiveness, good conductivity and large specific surface area, graphene is undoubtedly the most intriguing nanoscale substrate.

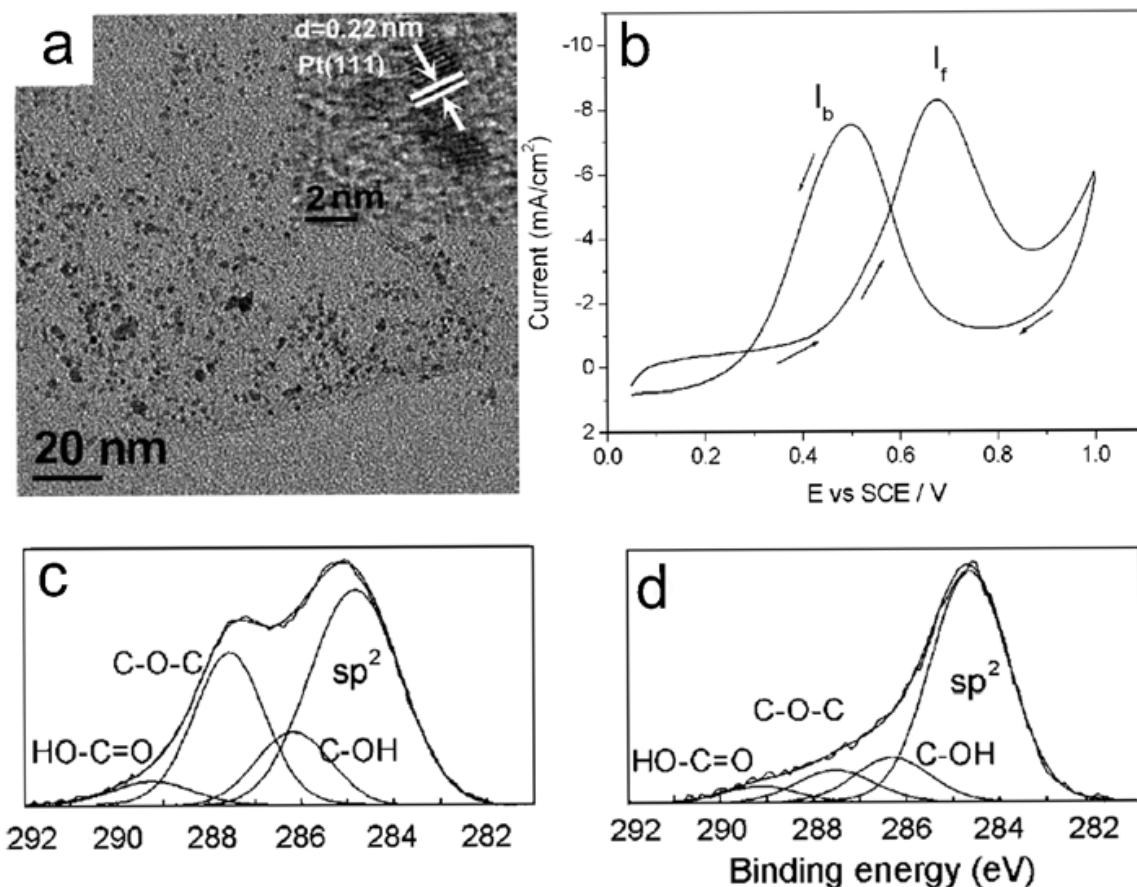


Fig. 10. (a) TEM images of graphene-Pt nanocomposites; (b) Cyclic voltammogram ( $20 \text{ mV s}^{-1}$ ) of methanol oxidation at graphene-Pt in  $2 \text{ M CH}_3\text{OH} + 1 \text{ M H}_2\text{SO}_4$  solution at room temperature. C1s XPS spectra of GO and graphene-Pt composite; (c) The C1s XPS spectrum of GO clearly indicates oxidation with four components that correspond to carbon atoms in different functional groups: the  $\text{sp}^2$ -hybridized C-C, the C in C-OH bonds, the epoxy C, and the carboxylate carbon; (d) the intensities of these groups in Pt-C become weak as a result of the deoxygenation, indicating the reduction of GO (Xu et al., 2008a).

Fig. 10 is the TEM, XPS and CV analyses of as-prepared graphene-Pt nanocomposites. It has been found that a water-ethylene glycol mixture is a very useful system to synthesize carbon-noble metal particle nanocomposites. Considering the facile exfoliation nature of GO in water, and the mild reducibility of the ethylene glycol for GO sheets, a water-ethylene glycol system was employed (Xu et al., 2008a). It is clearly seen in Fig. 10a that the almost transparent carbon sheets were decorated randomly by the nano-sized Pt particles. Because the monolayer carbon nanosheets were extremely thin, it was hard to make a distinction between them and the carbon-supported films on the copper grid. The crumpled silk waves of these carbon sheets leads us to believe that these nanoparticles indeed deposited on the supports. In addition, high-resolution TEM (HRTEM) images shown in the insets of Fig. 10a suggests the anchored crystal metal particles distributed uniformly on these single carbon sheets without obvious aggregations. The lattice fringes with interplanar distances of approximately 0.22 nm correspond to the nearest (111) plane of Pt.

The reduction of GO in water-ethylene glycol system can be verified by XPS analyses. The XPS spectrum of graphene-Pt composite indicates that the sample contains C, O and Pt as the main elements. The deconvolution of the C1s peak of graphene-Pt in Fig. 10d shows there are four types of carbon bonds: C-C (284.5 eV), C-OH (286.3 eV), C-O-C (287.5 eV), and HO-C=O (289.1 eV), respectively. By integrating the area of the deconvolution peaks, the following approximate percentages with respect to C-C bonds were obtained: C-C, 100; C-OH, 19; C-O-C, 14; HO-C=O, 6. The amount of incorporated functional groups in graphene-Pt is much lower than that of the unreduced GO as shown in Fig. 9c, where the approximate percentages of carbon atoms with respect to C-C bonds is C-C, 100; C-OH, 28; C-O-C, 59; HO-C=O, 11. The results of the XPS implied the decrease tendency of oxygen content in the composite. The intensity of some oxygenated functional groups on carbon sheets in the as-synthesized composites was obviously reduced, indicating the deoxygenation of GO. Specifically, the epoxy groups underwent considerable deoxygenation on the carbon sheets in these composites compared with the starting GO. The intensity of hydroxyl groups were also reduced to some extent.

The electrochemical performance of the graphene-Pt composite was tested for methanol oxidation, which is closely related to applications in DMFC. Figure 10b shows representative cyclic voltammetry plots of a graphene-Pt composite in CH<sub>3</sub>OH solution, in which the typical methanol oxidation current peaks ( $I_f$ , 0.68 V) and the residual carbon species oxidation peaks ( $I_b$ , 0.53 V) appeared. The ratio of  $I_f/I_b$  is high (1.35), suggesting the good CO toleration of the catalyst. Moreover, there is seldom change of  $I_f/I_b$  even after 50 cycles, indicating good stability in the electrochemical cycling process.

To further verify that graphene is a promising candidate as supports of high-loading metal catalyst in fuel cells, a composite of highly loaded 80 wt.% Pt-Ru on graphene sheets was prepared using colloidal method, using Vulcan XC-72R (a kind of active carbon with a surface area of  $\sim 250 \text{ m}^2 \text{ g}^{-1}$ ) for comparison (Bong et al., 2010). As displays in Fig. 11a, the TEM analyses were conducted to verify dispersion degree, particle size distribution, alloy state and average particle size of the catalyst. It is clearly seen that the almost transparent graphene sheets were decorated homogeneously by the nanoscale Pt-Ru alloy particles with excellent dispersion. The size of Pt-Ru particle on graphene sheets ranges from 1 to 3.5 nm with an average particle size of 2.5 nm (inlet of Fig. 11a). XRD data in Fig. 11b present Pt (1 1 1) peak observed from all alloy catalysts shifts slightly towards the higher values compared with the pure Pt. This shift means that the alloy is formed between Pt and Ru.

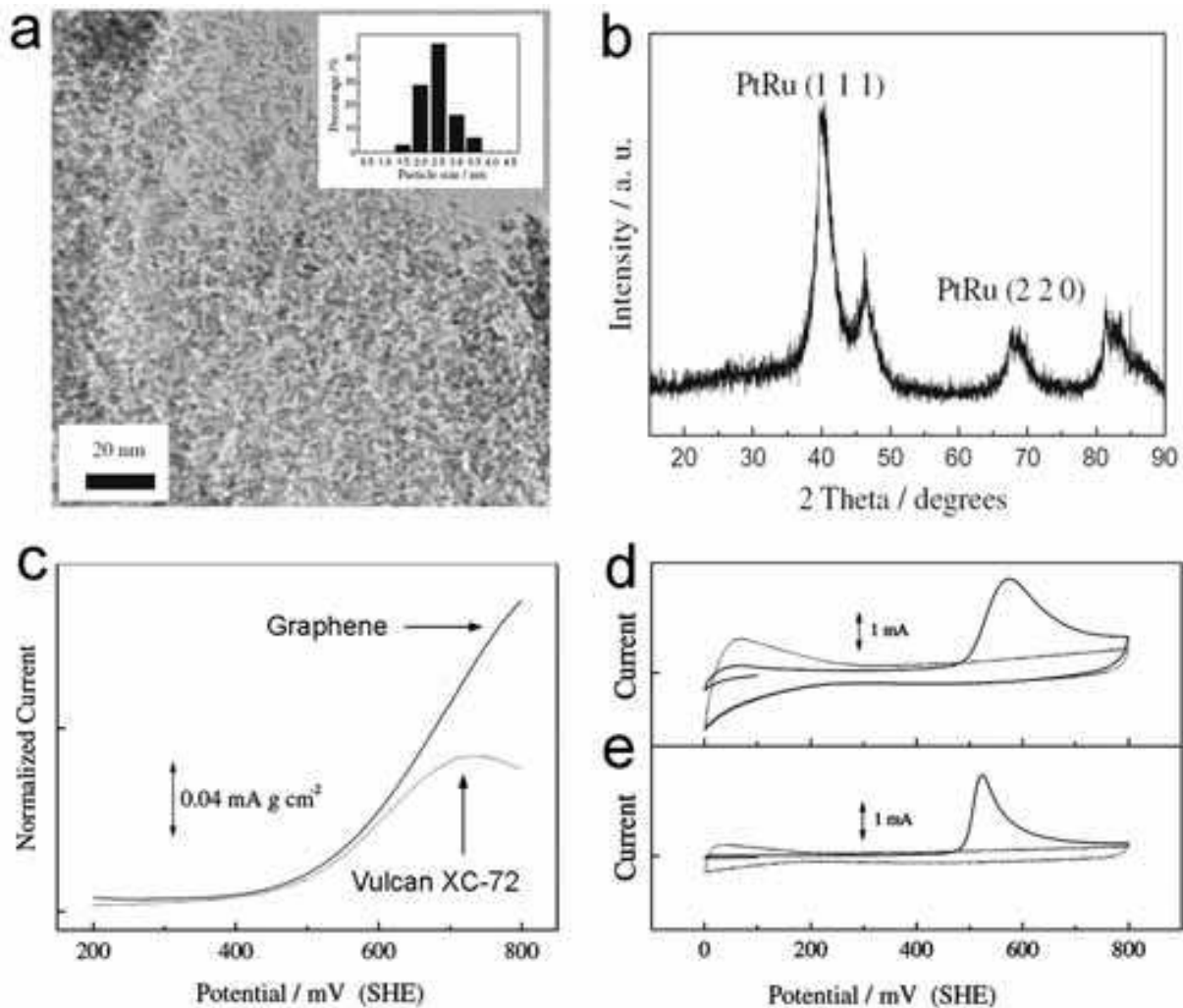


Fig. 11. (a) TEM images of Pt-Ru nanoparticles anchored on graphene sheets, and inset graph is particle size distribution of Pt-Ru/graphene; (b) XRD profile of Pt-Ru/graphene catalyst; (c) normalized linear sweep Voltammograms obtaining of graphene nanosheets and Vulcan XC-72 supported Pt-Ru catalyst in 1 M  $\text{H}_2\text{SO}_4$  and 1 M  $\text{CH}_3\text{OH}$  at 25 °C at a scan rate of 20  $\text{mV s}^{-1}$ ; (d)  $\text{CO}_{\text{ad}}$  stripping voltammograms of Pt-Ru/graphene and Pt-Ru/Vulcan XC-72 recorded in 1 M  $\text{H}_2\text{SO}_4$  at a scan rate of 20  $\text{mV s}^{-1}$  (Bong et al., 2010).

The electrochemically active surface area (ESA) is an effective manner to evaluate the number of available active sites. Fig. 11d and 11e shows the  $\text{CO}_{\text{ad}}$  stripping voltammograms of Pt-Ru/graphene and Pt-Ru/Vulcan recorded in 1 M  $\text{H}_2\text{SO}_4$  at a scan rate of 20  $\text{mV s}^{-1}$ . The ESA was determined assuming a monolayer of linearly adsorbed CO requires 420  $\mu\text{C cm}^{-2}$  for its oxidation interesting to note that graphene catalyst (47.9  $\text{m}^2 \text{g}^{-1}$ ) exhibits larger electrochemical surface area than Vulcan catalyst value (28.3  $\text{m}^2 \text{g}^{-1}$ ) and it is attributable to the size of Pt-Ru particles well anchored on graphene sheets. The difference of the ESA values is related to the difference in the particle size in inverse proportion. The electrocatalytic activity for methanol oxidation was evaluated by linear sweep voltammetry. Fig. 11c represents the linear sweep voltammogram of the Pt-Ru/graphene and Pt-Ru/Vulcan in 1M  $\text{CH}_3\text{OH}$  and 1 M  $\text{H}_2\text{SO}_4$  and the voltammogram displays that the Pt-Ru/graphene catalysts exhibit almost four times higher geometric anode peak current than that of Pt-Ru/Vulcan. In addition, these results can be transferred into normalized current

density ( $\text{mA g m}^{-2}$ ). Considering the electrochemical surface area and those of Pt-Ru/graphene and Pt-Ru/Vulcan are 0.113 and 0.0812  $\text{mA g m}^{-2}$  at 700 mV, respectively. The enhancement of electrochemical activity of Pt-Ru/graphene could originate from highly dispersed particle size effect and large electrochemical surface area.

## 2.6 Supercapacitors

In recent years, due to environmental issues and depleting fossil fuels, interest in the development of alternative energy storage/conversion devices with high power and energy densities catering to the present day demands has increased to a great extent. Supercapacitors, also named electrochemical capacitors (ECs) or ultracapacitors, is a novel, low-cost and environmentally friendly energy storage systems. One of its advantage is that it can store and release energy at relatively higher rates than those accessible with batteries because its mechanisms for energy storage. In addition, they have several orders of magnitude higher energy density than that of conventional dielectric capacitors. They can complement or replace batteries in electrical energy storage and harvesting applications, when high power delivery or uptake is needed. Since 1957, when the practical utilization of electrochemical capacitors for the storage of electrical charge was demonstrated and patented by General Electric, supercapacitors are ideal for any application having a short load cycle and high reliability requirement, such as energy recapture sources including load cranes, forklifts, and electric vehicles.

Commonly, a supercapacitor unit cell is composed of two porous electrodes that are isolated from electrical contact by a separator (Fig. 12a). Current collectors of metal foil or carbon impregnated polymers are employed to conduct electrical current from each electrode. The separator and the electrodes are impregnated with an electrolyte, which allows ionic current to flow between the electrodes while preventing electronic current from discharging the cell. A packaged supercapacitor module, depending upon the desired size and voltage, is constructed of multiple repeating unit cells (Stoller et al., 2008). To approach the real application, the coin-shaped supercapacitors have been fabricated. An optical image of a real coin-shaped graphene-based supercapacitor device is displayed in Figure 12c (Wang et al., 2009b).

Generally, there are two kinds of supercapacitors based on the electrode materials: (1) high surface area, inert and conductive materials that store and release energy by nanoscopic charge separation at the electrochemical interface between an electrode and an electrolyte; (2) some redox active materials that use fast, reversible redox reactions at the surface of active materials which is known as the pseudo-capacitance. The carbonaceous nanostructures (like CNTs, active carbon and graphene) are commonly studied as electrodes for electrochemical double layer capacitors (EDLCs); while transition metal oxides or hydroxides (such as  $\text{RuO}_2$ ,  $\text{MnO}_2$ ,  $\text{Ni(OH)}_2$ , etc.) and conducting polymers (like polyaniline), are promising material for pseudocapacitors.

Considering that graphene sheets have high electrical conductivity and large specific surface area (calculated value,  $2630 \text{ m}^2 \text{ g}^{-1}$ ), which is substantially higher than values derived from BET surface area measurements of other carbon supports (such as activated carbons, carbon fibers, and CNTs), these peculiar characters may beneficial for insertion/desertion between ions of electrolyte and electrode material, giving rise to the good electrochemical performance of the material. The utilization of individual graphene sheets as electrode material for supercapacitors has been reported. Fig. 12b is the TEM images of graphene sheets prepared from a solution reduction process. It is interesting that this unique structure

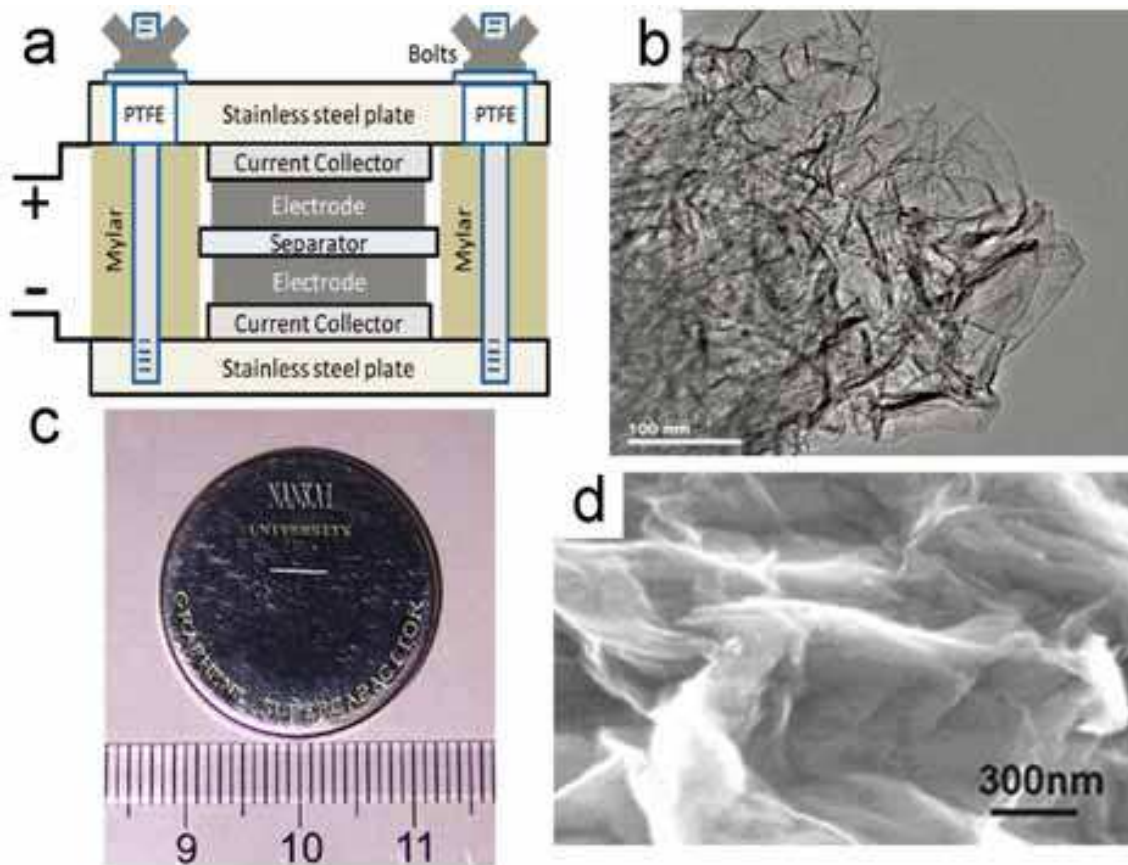


Fig. 12. (a) Schematic of test cell assembly of supercapacitors (Stoller et al., 2008); (b) TEM images of graphene sheets prepared from a solution reduction process (Stoller et al., 2008); (c) An optical image of an industry-grade coin-shaped graphene-based supercapacitor device (Wang et al., 2009b); (d) Scanning electron microscopy (SEM) image graphene sheets prepared from gas-based hydrazine reduction (Wang et al., 2009b).

gives graphene a consistently good performance over a wide range of voltage scan rates in the electrochemical testing (Stoller et al., 2008). In addition, Wang et al proposed a procedure for preparing graphene from gas-based hydrazine reduction of GO, which could restore the conducting carbon network without yielding much aggregation. SEM image of as-obtained graphene sheets is shown in Figure 12b. Notably that the graphene material exhibit excellent stability, with specific capacitance remaining ~90 % after 1200 cycles (Wang et al., 2009b).

Despite these advantages, graphene, being a kind of carbon material and charged-discharged mainly by EDLC, is also subjected to the problems that have emerged in other carbon-based materials for supercapacitors. The utilization of strong alkaline electrolyte is less eco-friendly. The specific capacitance of the pure graphene-based devices is relatively low in comparison with that of other pseudocapacitive materials, resulting in a low energy density. For example, the specific capacitance of graphene ranges from 100 to 200  $F g^{-1}$ , while as a typical metal oxide, hydrate  $RuO_2$ , has a specific capacitance of 720  $F g^{-1}$ . A notable improvement in performance may be achieved through the advances in understanding charge storage mechanisms and the development of advanced nanostructured materials. In view of large specific area, good conductivity and excellent electrochemical stability of graphene, and high power density of pseudo-captive materials,

one possible route to acquire high-performance electrochemical materials is the combination of graphene and the pseudocapacitive materials. Moreover, it should be mentioned that due to the low natural abundance and the requirement of highly acidic solutions in operation (such as sulfuric acid) as electrolyte have limited wide spread usage of  $\text{RuO}_2$ , and therefore, the development of novel electrode materials will accelerate the supercapacitor having an energy density as high as a secondary battery.

### 2.6.1 Graphene-inorganic nanoparticles composites

Manganese dioxide ( $\text{MnO}_2$ ) is one of the most stable manganese oxides with excellent physical and chemical properties under ambient conditions. Because of its rich polymorphism and structural flexibility, this oxide has wide applications in catalysis, ion exchange, molecular absorption, microwave absorption, biosensors, and energy storage. As a potential excellent electrode material for the alternation of  $\text{RuO}_2$  in supercapacitors,  $\text{MnO}_2$  has received considerable attention in recent years owing to its abundant availability on the earth. Besides,  $\text{MnO}_2$  shows good electrochemical performance in a neutral electrolyte (such as  $\text{Na}_2\text{SO}_4$ ,  $\text{K}_2\text{SO}_4$ , and  $\text{LiCl}$ ), which would be noteworthy when focused on eco-friendly point of view. As recently demonstrated, the electrochemical performance of  $\text{MnO}_2$  critically depends on their crystallographic forms and then on their textural properties including morphology, surface area, pore volume, pore dimension, etc (Devaraj & Munichandraiah, 2008).

Considering the abundant functional groups of GO which can be regarded as anchor sites, a study on using GO as nanoscale supports to stabilize  $\text{MnO}_2$  particles is examined (Chen et al., 2010d). Take the composite of  $\text{CMG}_3$  (chemically synthesized GO- $\text{MnO}_2$  nanocomposites when the feeding ratio of  $\text{MnO}_2/\text{GO}$  is 3/1; the mass of  $\text{MnO}_2$  is calculated by  $\text{MnCl}_2$  according to the reaction:  $2\text{KMnO}_4 + 3\text{MnCl}_2 + 2\text{H}_2\text{O} \rightarrow 5\text{MnO}_2 + 2\text{KCl} + 4\text{HCl}$ ) as an example. The results of nanocomposites with other feeding ratios are similar. The heterostructure of the composite is shown in Fig. 13. The GO sheets are multi-layers with diameters of a few micrometers, while the nano- $\text{MnO}_2$  shows needle-like morphology with typical diameters of 20-50 nm and lengths of 200-500 nm. It can be clearly seen from Figure 13c that the GO sheets were exfoliated and decorated randomly with the needle-like  $\text{MnO}_2$ . Comparing the bright- and dark-field TEM images in Figure 13c and d, the single layered graphene oxide sheet can be clearly distinguished from the background. The tip of a  $\text{MnO}_2$  nanoneedle is shown in Figure 13e and f. It can be clearly seen from Figure 13e that the nanoneedle is actually composed of a few primary nanorods aggregated along the lateral faces. The nanorods of the center portions are longer than others, giving an indication that the oriented attachment mechanism played an important role in the formation of the nanoneedles. Additionally, the lattice fringes with interplanar distances of approximately 0.7 nm shown in Figure 13f correspond to the (110) plane of the tetragonal  $\alpha$ - $\text{MnO}_2$  structure.

To test the electrochemical properties of GO- $\text{MnO}_2$  composites, the samples were fabricated into electrodes and characterized with CV and galvanostatic charge-discharge measurements. CV response carried out at a scan rate of  $5 \text{ mV s}^{-1}$  in 1 M  $\text{Na}_2\text{SO}_4$  aqueous electrolyte solution is shown in Figure 14. The rectangular and symmetric CV curves of nano- $\text{MnO}_2$  indicate the ideal pseudo-capacitive nature of the fabricated electrode, while the lack of symmetry in  $\text{CMG}_{0.5}$ ,  $\text{CMG}_3$ , and  $\text{CMG}_{15}$  is probably due to combined double-layer and pseudo-capacitive contribution to the total capacitance. Interestingly, with the feeding ratio of  $\text{MnO}_2/\text{GO}$  increasing from 0.5 to 15, CV plots of  $\text{CMG}_{\text{ratio}}$  became more close to that of the nano- $\text{MnO}_2$ , which can be attributed to the increment of pseudo-capacitive contribution to the overall capacitance.

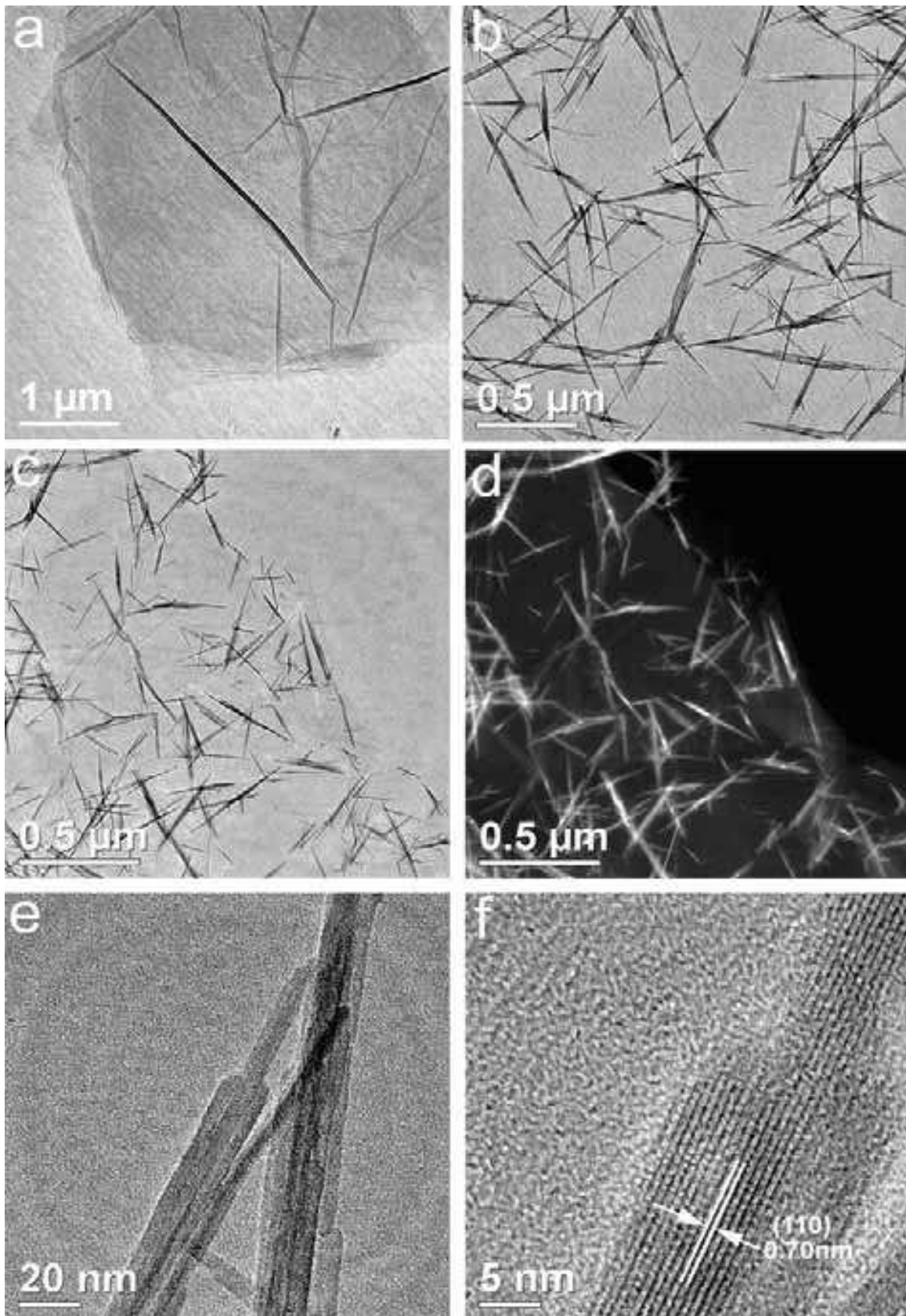


Fig. 13. (a, b) TEM images of GO and nano-MnO<sub>2</sub>; (c, d) Bright and dark field images of CMG<sub>3</sub>; (e, f) the HRTEM images of a MnO<sub>2</sub> nanoneedle (Chen et al., 2010d).

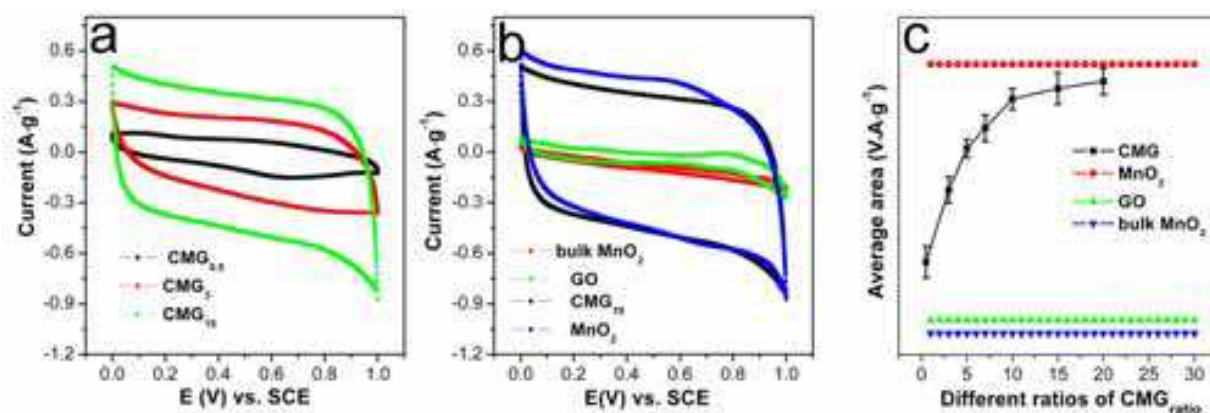


Fig. 14. CVs of (a) CMG<sub>0.5</sub>, CMG<sub>3</sub>, CMG<sub>15</sub>; (b) bulk MnO<sub>2</sub>, GO, CMG<sub>15</sub> and nano-MnO<sub>2</sub> at 5 mV s<sup>-1</sup> in 1 M Na<sub>2</sub>SO<sub>4</sub> solution; (c) Plot of average area of CV curves as a function of different ratios of CMG<sub>ratio</sub>, with the average area of CV curves of nano-MnO<sub>2</sub>, GO, and bulk MnO<sub>2</sub> for comparison (Chen et al., 2010d).

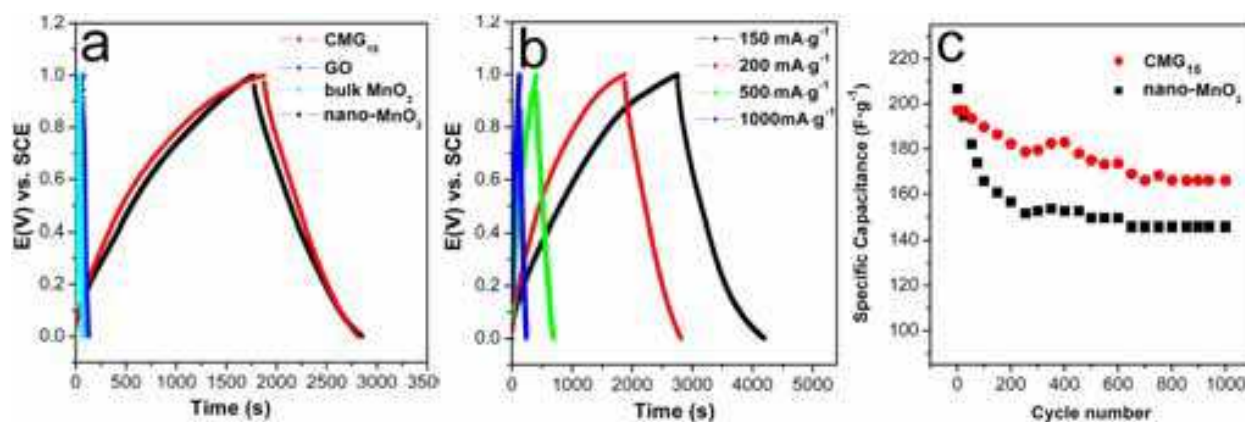


Fig. 15. CVs of (a) CMG<sub>0.5</sub>, CMG<sub>3</sub>, CMG<sub>15</sub>; (b) bulk MnO<sub>2</sub>, GO, CMG<sub>15</sub> and nano-MnO<sub>2</sub> at 5 mV s<sup>-1</sup> in 1 M Na<sub>2</sub>SO<sub>4</sub> solution; (c) Plot of average area of CV curves as a function of different ratios of CMG<sub>ratio</sub>, with the average area of CV curves of nano-MnO<sub>2</sub>, GO, and bulk MnO<sub>2</sub> for comparison (Chen et al., 2010d).

Galvanostatic charge-discharge measurements were carried out in 1 M Na<sub>2</sub>SO<sub>4</sub> at a current density of 200 mA g<sup>-1</sup>. As illustrated in Figure 15a, during the charging and discharging steps, the charge curve of CMG<sub>15</sub> is almost symmetric to its corresponding discharge counterpart with a slight curvature, indicating the pseudo-capacitive contribution along with the double layer contribution. The  $C_s$  is calculated according to  $C_s = I \times \Delta t / \Delta V \times m$  from the discharge curves, where  $I$  is the constant discharge current,  $\Delta t$  is the discharge time,  $\Delta V$  is the potential drop during discharge; the  $C_s$  values of CMG<sub>15</sub>, nano-MnO<sub>2</sub>, GO and bulk MnO<sub>2</sub> are 197.2, 211.2, 10.9, and 6.8 F g<sup>-1</sup>, respectively. These values are mainly consistent with the order indicated by the CVs.

Furthermore, the electrochemical stability of CMG<sub>15</sub> and nano-MnO<sub>2</sub> is investigated in the range of 0 to 1 V at 200 mA g<sup>-1</sup> in 1 M Na<sub>2</sub>SO<sub>4</sub> aqueous solution (Figure 14c). It is found that the CMG<sub>15</sub> electrode retained about 84.1 % (165.9 F g<sup>-1</sup>) of initial capacitance after 1000 cycles, while that of the nano-MnO<sub>2</sub> retained only about 69.0 % (145.7 F g<sup>-1</sup>). The discrepant electrochemical stability between CMG<sub>15</sub> and nano-MnO<sub>2</sub> may be attributable to the different double-layer and pseudo-capacitive contributions. As well known, the double-

layer process only involves a charge rearrangement, while pseudo-capacitive is related to a chemical reaction, and the double-layer capacitors have a better electrochemical stability but lower  $C_s$  as compared with those of pseudo-capacitors. Accordingly, the as-synthesized CMG<sub>15</sub>, making more double-layer contribution compared to that of nano-MnO<sub>2</sub> owing to the effect of GO, have a slightly lower  $C_s$  than the later; however, the electrochemical stability is obviously enhanced.

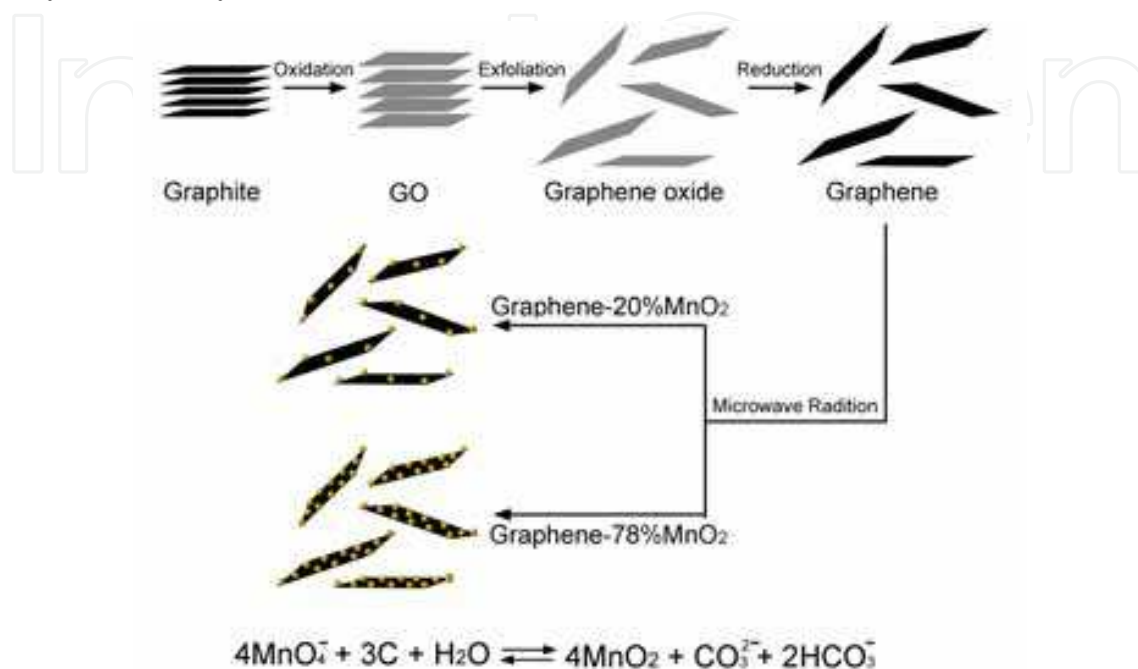


Fig. 16. Schematic illustration and possible reactions for the synthesis of graphene-20% MnO<sub>2</sub> and graphene-70% MnO<sub>2</sub> composites (Yan et al., 2010).

As mentioned in chapter 3.3, the deoxygenation of GO-MnO<sub>2</sub> by reducing agent (like ethylene glycol) only produces graphene-MnOOH composites. To prepare the hybrid of graphene supported MnO<sub>2</sub> nanoparticles, the redox reaction between graphene sheets and KMnO<sub>4</sub> by microwave irradiation was reported (Yan et al., 2010). The schematic illustration and possible reactions for the synthesis of graphene-20% MnO<sub>2</sub> and graphene-70% MnO<sub>2</sub> composites are shown in Fig. 16. It can be seen from SEM and TEM images that graphene nanosheets can serve mainly as a highly conductive support, which can also provide a large surface for the deposition of nanoscale MnO<sub>2</sub> particles of about 5–10 nm (not shown). The large surface of graphene has been preserved by the products. The excellent interfacial contact and increased contact area between MnO<sub>2</sub> and graphene can significantly promote the electrical conductivity of the electrode due to the high electrical conductivity of graphene. Besides, the easy surface accessibility of this composite by the electrolyte, and the improved electrochemical utilization of MnO<sub>2</sub>, resulted from the small particle size and high surface/area of the oxides, could provide both the high reversible pseudo-capacity and excellent capacitive retention ratio at high charge-discharge rate. In addition, the electrochemical tests of the as-obtained products show excellent performances. Graphene-78 wt.% MnO<sub>2</sub> composite displays the specific capacitance as high as 310 F g<sup>-1</sup> at 2 mV s<sup>-1</sup>, which is almost three times higher than that of pure graphene (104 F g<sup>-1</sup>) and birnessite-type MnO<sub>2</sub> (103 F g<sup>-1</sup>). The capacitance retention ratio is highly kept over a wide range of scan rates (88% at 100 mV s<sup>-1</sup> and 74% at 500 mV s<sup>-1</sup>). Moreover, the electrode material has a low ESR of ~0.66 Ω and good stability.

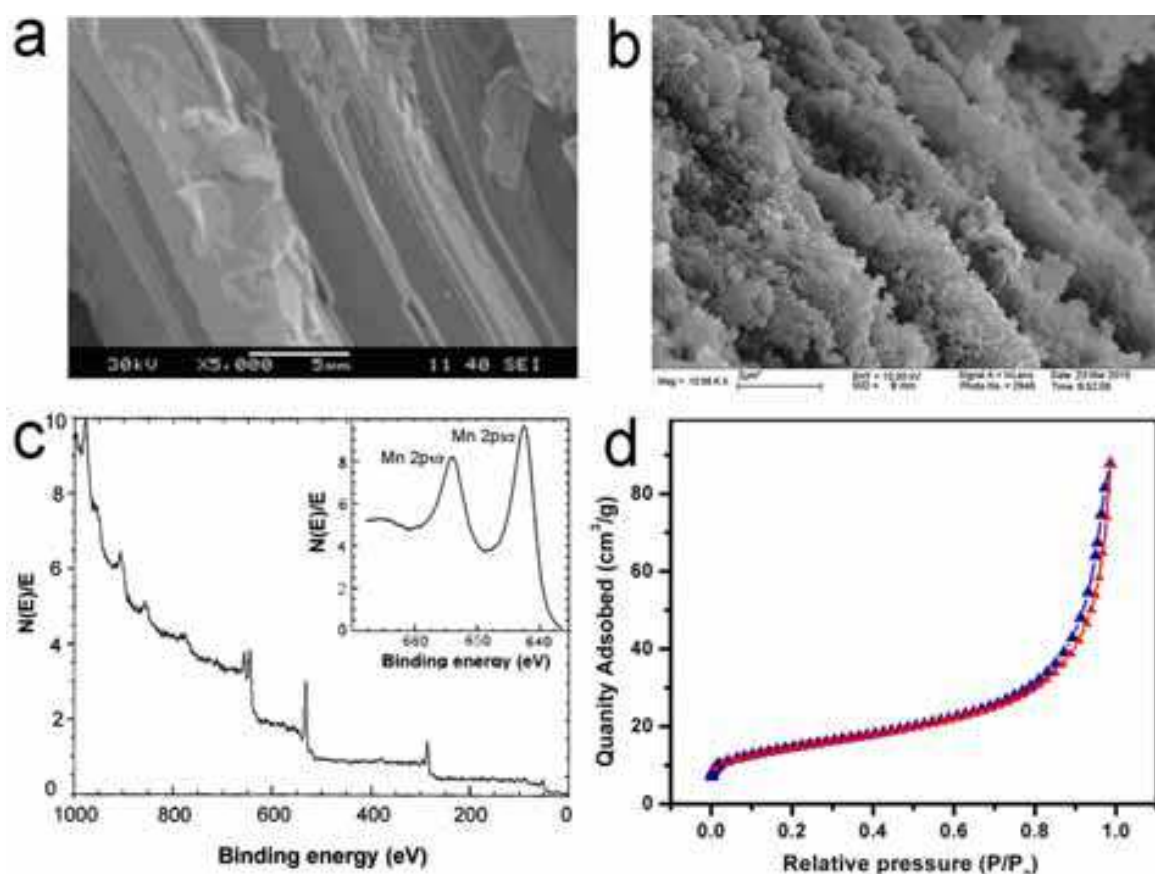


Fig. 17. (a) FESEM images of graphene sheets; (b) FESEM (c) XPS (d) Nitrogen adsorption/desorption isotherm of the as-obtained  $\text{MnO}_2$ -lamellas. The inset of (a) is the digital image of graphene dispersion; the inset of (c) is Mn (2P) peaks of  $\text{MnO}_2$  nano-lamellas in XPS analyses (Chen et al., 2010c).

To further enrich potential applications of graphene, a facile procedure to explore the framework substitution of graphene by  $\text{MnO}_2$  is investigated (Chen et al., 2010c). Single-layer-graphene and few-layer-graphene structures have been predicted to have high specific surface area. Recent research has focused largely on utilizing the intriguing morphology of graphene as building blocks or substrates, keeping the structure undisturbed. Therefore, a procedure for morphology transmission from graphene to  $\text{MnO}_2$  nano-lamellas by in situ replacement with the framework of graphene is examined. The approach involves using graphene sheets as the starting reagent, thereby transmitting the morphology of layered structure from graphene to as-prepared  $\text{MnO}_2$  product.

The definitive evidence that almost all the carbon atoms of graphene can be replaced by  $\text{MnO}_2$  to form nano-lamellas was obtained with FESEM. It can be seen in Fig. 17 that the lamellar structure of graphene was indeed transmitted to the products. The brinks of the sheets can be clearly discerned; the lamellar structures of the products are fully seen. XPS results (Fig. 17c) indicate that the product contains Mn and O as the main components, while C and K are impurities. The binding energy of Mn 2p<sub>1/2</sub> and Mn 2p<sub>3/2</sub> is 642.4 and 654.2 eV, respectively. The splitting of the Mn 2p peak (11.8 eV) is very close to that of manganese (+4), suggesting the  $\text{MnO}_2$  nature of the product. Surface area measurements indicate that the  $\text{MnO}_2$  nano-lamellas have a Brunauer-Emmett-Teller (BET, nitrogen, 77 K) surface area of 50.3 m<sup>2</sup> g<sup>-1</sup>, with pore volume of 0.135 cm<sup>3</sup> g<sup>-1</sup>, and BJH desorption average

pore diameter of 14.4 nm. Remarkably, this value is much higher than the  $\text{MnO}_2$  produced by traditional co-precipitation of  $\text{KMnO}_4$  and  $\text{Mn}^{2+}$ . A large surface area suggests wider utilization of the as-prepared material.

The as-prepared products were fabricated to electrodes and tested using CV and galvanostatic charge/discharge measurements in 1 M  $\text{Na}_2\text{SO}_4$  aqueous electrolyte (Figure 17). The rectangular and symmetric CV curves of  $\text{MnO}_2$  nano-lamellas in Figure 15a indicate the ideal pseudo-capacitive nature of the as-fabricated electrode, while the lack of symmetry in graphene can be attributed to its double-layer capacitance in neutral electrolyte. Specific capacitance of  $\text{MnO}_2$  calculated at 150, 200, 500, 1000 and 2000  $\text{mA g}^{-1}$  from the discharge curves is 206.2, 200.1, 191.0, 165.8 and 149.7  $\text{F g}^{-1}$ , respectively (Figure 18b-c). About 72.6 % specific capacitance was retained even with the current density increasing from 150 to 2000  $\text{mA g}^{-1}$ . Consistently good performance of  $\text{MnO}_2$  nano-lamellas over a wide range of current densities suggests this material is promising as supercapacitor electrodes. Additionally, when the charge-discharge was cycled at 500  $\text{mA g}^{-1}$  as shown in Figure 18d, there is only a slight decrease in capacitance of less than 10 % even after 3000 cycles, demonstrating a great stability.

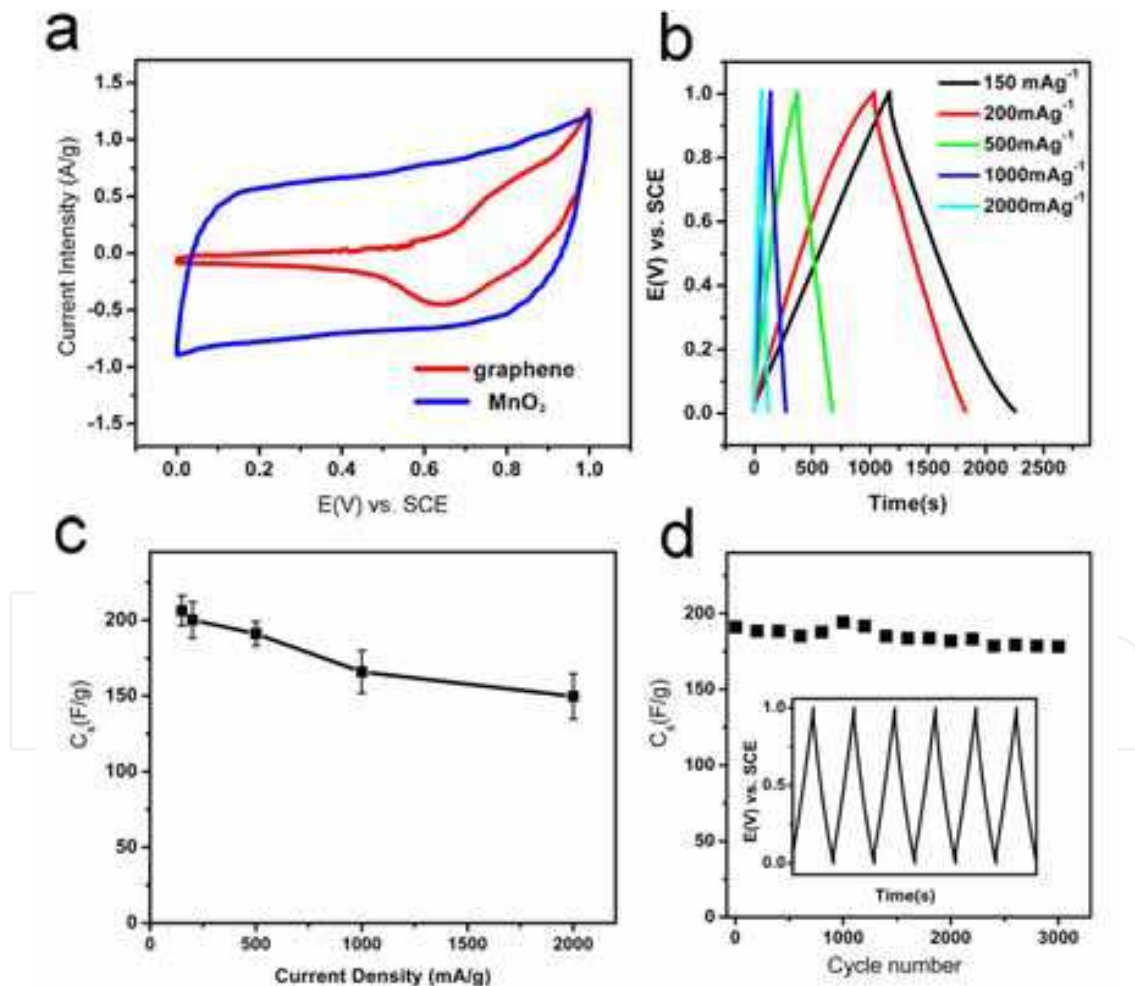


Fig. 18. (a) CV plots of graphene and  $\text{MnO}_2$  at 5  $\text{mV s}^{-1}$ ; (b) Galvanostatic charge/discharge measurements of  $\text{MnO}_2$  nano-lamellas at different current densities; (c) Plot of specific capacitance ( $C_s$ ) as a function of current density of  $\text{MnO}_2$  lamellas; (d) Cycle life of  $\text{MnO}_2$  lamellas at 500  $\text{mA g}^{-1}$  (Chen et al., 2010c).

Besides  $\text{MnO}_2$ , It has been demonstrated that some other metal oxides, such as  $\text{SnO}_2$ ,  $\text{ZnO}$  (Lu et al., 2010) and  $\text{Mn}_3\text{O}_4$  (Wang et al., 2010) etc., are also promising candidates as electrode material for supercapacitors. Specifically, recent studies suggest transitional metal hydroxides, such as  $\text{Co}(\text{OH})_2$  or  $\text{Ni}(\text{OH})_2$ , have shown advanced electrochemical behaviors. Cobalt Hydroxide ( $\text{Co}(\text{OH})_2$ ) is an attractive material in recent years on account of their layered structure with large interlayer spacing and their well-defined electrochemical redox activity. Being an important electrochemical active material, a great deal of interest has been centered on the utilizations of  $\text{Co}(\text{OH})_2$  material in alkaline batteries, fuel cells and supercapacitors. Previous reports have shown that the film of  $\text{Co}(\text{OH})_2$  material has a higher specific capacitance than that of  $\text{RuO}_2$ . Taking into account the high specific area of graphene which be serve as excellent building blocks for nanocomposites, and the fact that graphene is a promising supercapacitor electrode material, consistently giving good electrochemical performance in strong alkaline electrolytes, the combination of  $\text{Co}(\text{OH})_2$  and graphene may produce synergistic results, giving the overall system enhanced electrochemical properties.

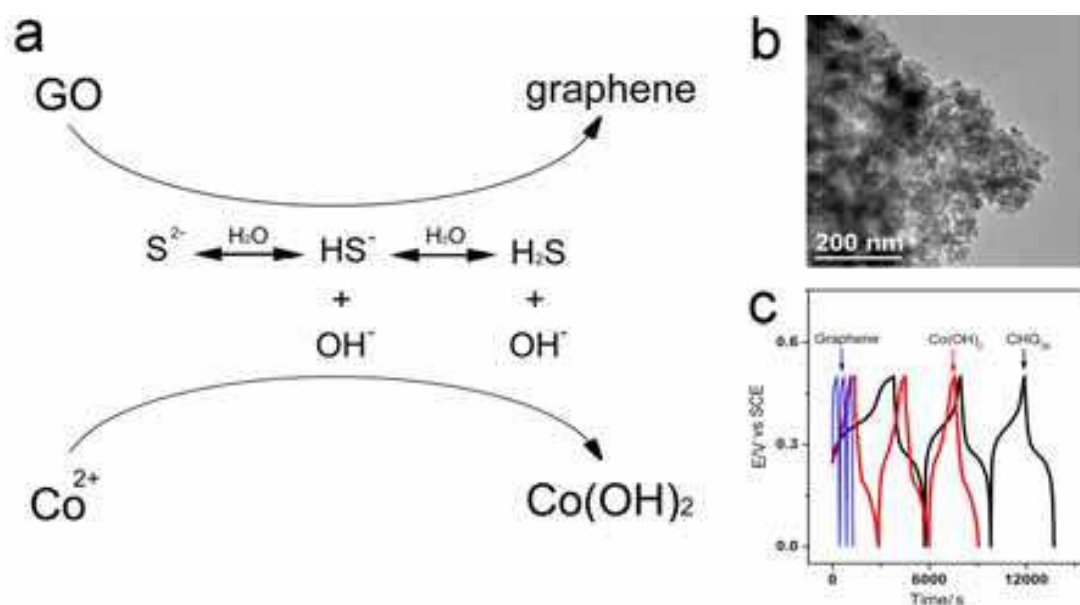


Fig. 19. (a) Proposed reactions for the formation of graphene- $\text{Co}(\text{OH})_2$  nanocomposites; on one hand deoxygenate GO by  $\text{S}^{2-}$ ,  $\text{HS}^-$ ,  $\text{H}_2\text{S}$ , and  $\text{OH}^-$  from hydrolyzation of  $\text{Na}_2\text{S}$  in aqueous solution, on the other hand deposit  $\text{Co}^{2+}$  by  $\text{OH}^-$  (Chen et al., 2010b).

A typical procedure of depositing  $\text{Co}(\text{OH})_2$  onto graphene sheets is depicted in Fig. 19a. One essential characteristic of this procedure is the utilization of in situ hydroxylation of  $\text{Na}_2\text{S}$  aqueous solutions (Chen et al., 2010b). Due to the strong inclination of  $\text{Na}_2\text{S}$  to be hydrolyzed in aqueous solutions, the deposition of  $\text{Co}^{2+}$  and deoxygenation of GO occur in one step. Specifically, the negatively charged GO sheets, which have a high capability of absorbing dissolved  $\text{Co}^{2+}$  ions via electrostatic interactions, were first suspended in isopropanol. Subsequently,  $\text{Na}_2\text{S}$  aqueous solution was introduced rapidly into the above system. Due to the formation of large amounts of  $\text{OH}^-$  produced by the hydrolysis of  $\text{Na}_2\text{S}$ ,  $\text{Co}^{2+}$  was precipitated easily in the form of  $\text{Co}(\text{OH})_2$ . The exhaustion of  $\text{OH}^-$  provides a strong driving force for the further hydrolysis of  $\text{Na}_2\text{S}$ , which leads to the releasing of  $\text{H}_2\text{S}$  in large amounts. On the other hand, the produced  $\text{H}_2\text{S}$ , along with  $\text{HS}^-$ ,  $\text{S}^{2-}$  and  $\text{OH}^-$  provide a great boost to the deoxygenation of GO.

Figure 19b displays a high density of  $\text{Co(OH)}_2$  on graphene sheets for  $\text{CHG}_{30}$  (chemically synthesized from graphene- $\text{Co(OH)}_2$  nanocomposites at a feeding ratio of 30/1 for  $\text{Co(OH)}_2/\text{GO}$ ;  $\text{Co(OH)}_2$  is calculated on the basis of the amount of  $\text{CoCl}_2 \cdot 6\text{H}_2\text{O}$  utilized according to the reaction:  $\text{Co}^{2+} + 2\text{OH}^- \rightarrow \text{Co(OH)}_2$ ), and it looks like the particles are enveloped by a thin film. Notably, the graphene sheets are exfoliated and serve as excellent substrates to stabilize  $\text{Co(OH)}_2$ .

Figure 19c shows galvanostatic charge-discharge curves of  $\text{CHG}_{30}$ ,  $\text{Co(OH)}_2$ , and graphene at  $500 \text{ mA g}^{-1}$ . The  $C_s$  of  $\text{CHG}_{30}$ ,  $\text{Co(OH)}_2$ , and graphene at  $500 \text{ mA g}^{-1}$  are calculated to be 972.5, 726.1, and  $137.6 \text{ F g}^{-1}$ , respectively. The higher  $C_s$  of  $\text{CHG}_{30}$  than that of individual  $\text{Co(OH)}_2$ , and graphene suggests an elevated electrochemical performance of the overall system. Notably, the  $C_s$  value of  $\text{CHG}_{30}$  ( $972.5 \text{ F g}^{-1}$ ) is obviously higher than the typical electrode material of supercapacitors ( $\text{RuO}_2$ ,  $720 \text{ F g}^{-1}$ ), implying good electrochemical capacitance behaviors of the as-prepared nanocomposite.

Additionally, as reported by Wang et al. (Wang et al., 2010a), Single-crystalline  $\text{Ni(OH)}_2$  hexagonal nanoplates directly grown on lightly oxidized, electrically conducting graphene sheets has exhibited advanced electrochemical performances, with high specific capacitance of  $\sim 1335 \text{ F g}^{-1}$  at a charge and discharge current density of  $2.8 \text{ A g}^{-1}$  and  $\sim 953 \text{ F g}^{-1}$  at  $45.7 \text{ A g}^{-1}$  with excellent cycling ability. It is highlighted the importance of direct growth of nanomaterials on graphene to impart intimate interactions and efficient charge transport between the active nanomaterials and the conducting graphene network. Considering the low cost of Mn, Co and Ni in comparison with noble metals (Ru), the advancement in these fields has stimulated significant progresses in supercapacitors.

### 2.6.2 Graphene-poly aniline (PANI) composites

Among the families of electrode materials for supercapacitors, conductive polymers have been extensively studied in recent years. Owing to the pseudocapacitive behaviors in doping and dedoping process, these materials could give large specific capacitance, high power and energy density. The main conductive polymer materials that have been investigated for the supercapacitor electrode are polyaniline (PANI), polypyrrole (PPy), polythiophene (PTH) and their derivatives, and so on. Polyaniline (PANI) is a popular due to its ease of synthesis, environmental stability, and simple acid-doping/base-dedoping chemistry. However, the relative poor cycling life restricts its practical applications. Taking into the good electrochemical stability of carbons (like graphene), the combination of graphene with PANI may provide improved performances as electrode materials for supercapacitors.

Considering the hydrophilic nature of GO, a simple in situ polymerization method in water system was reported to synthesize the nanocomposites of GO-doped PANI (GP) which were used as electrode materials (Wang et al., 2009a). The nanocomposites, signed as  $\text{PG}_{\text{ratio}}$ , like  $\text{PG}_{100:1}$ ,  $\text{PG}_{61:1}$ , represent the feeding ratios of PANI: GO.

SEM and TEM images in Fig. 20e and f demonstrate the fibrillar morphology of the prepared nanocomposite  $\text{PG}_{100:1}$ , with the dimension of about 300 nm in diameter and 2-3  $\mu\text{m}$  in length, compared with the granular aggregate structure for the pure PANI (not shown). These fibers are in fact built from many smaller nanofibers about 30 nm in diameter and 100-150 nm in length on the surface, and nanosheets in the backbone of the fibers.

Fig. 20a and b illustrates the cyclic voltammograms (CVs) and EIS plots of PANI, GO,  $\text{PG}_{61:1}$  and  $\text{PG}_{100:1}$  electrode. Compared with the GO and PANI electrodes, the nanocomposites exhibit larger current density response in  $\text{A g}^{-1}$  at  $10 \text{ mV s}^{-1}$  and less estimated charge-transfer resistances. This means that the electrochemical performances of the nanocomposites are enhanced due to the synergistic effect between GO and PANI.

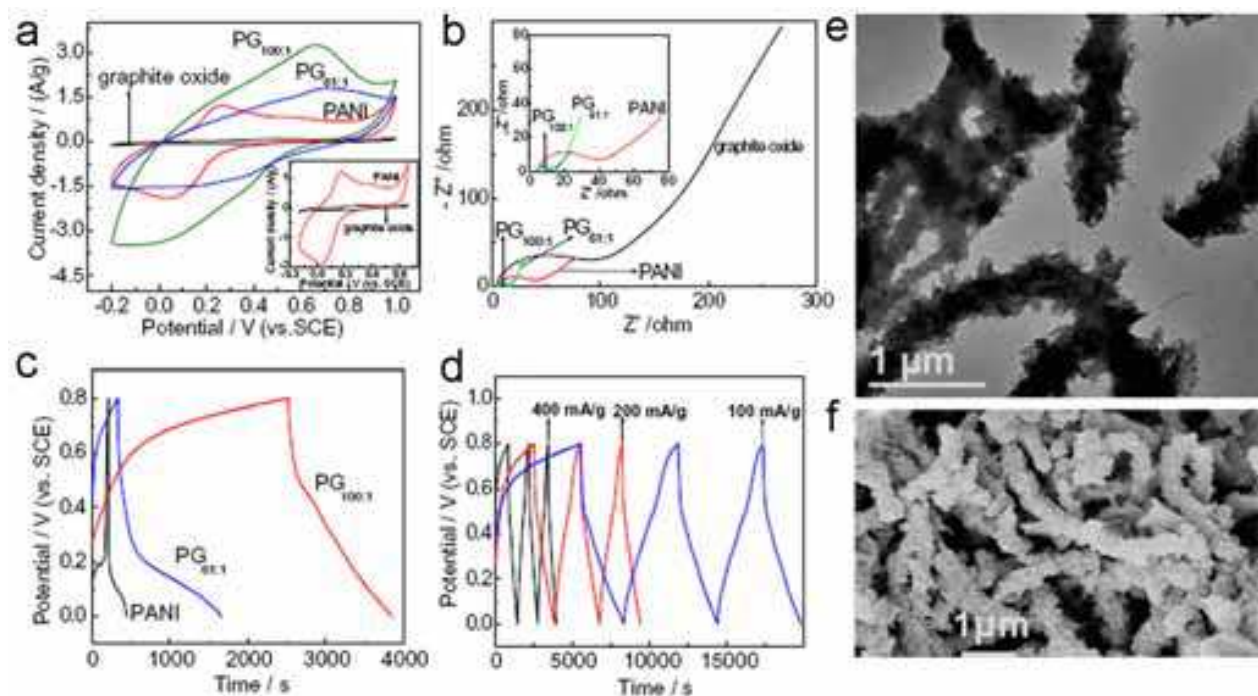


Fig. 20. CVs (a) at  $10 \text{ mV s}^{-1}$  (b) EIS of GO, PANI,  $\text{PG}_{61:1}$ ,  $\text{PG}_{100:1}$ ; (c) galvanostatic charge-discharge curves of PANI,  $\text{PG}_{61:1}$ ,  $\text{PG}_{100:1}$  at  $200 \text{ mA g}^{-1}$ ; (d) galvanostatic charge-discharge curves of  $\text{PG}_{100:1}$  at 100, 200, and  $400 \text{ mA g}^{-1}$ , respectively; TEM (e) and SEM (f) images of  $\text{PG}_{100:1}$  (Wang et al., 2009a).

The specific capacitance ( $C_s$ ) was calculated from the charging and discharging curves (Fig. 20c). The high  $C_s$  values were evaluated as 216, 284 and  $531 \text{ F g}^{-1}$  at  $200 \text{ mA g}^{-1}$  in the range from 0 to 0.45 V, for PANI,  $\text{PG}_{61:1}$  and  $\text{PG}_{100:1}$ , respectively. Remarkably, the capacitance of the polymeric material is critically enhanced by the GO sheets. Moreover, the nanocomposites demonstrate good capacitive behavior and charge-discharge property at a current density of  $100\text{-}500 \text{ mA g}^{-1}$ .  $C_s$  of  $\text{PG}_{100:1}$  is higher and that of  $\text{PG}_{61:1}$ , implying that the feeding ratio of the nanocomposite influences its electrochemical capacitance greatly.

The possible combining mode of GO/PANI composite is investigated using Raman, FTIR, UV-vis and XPS, which is proposed including: (a)  $\pi$ - $\pi$  stacking (b) electrostatic interactions, and (c) hydrogen bonding, as presented in Fig. 21 (Wang et al., 2010b).

Because the reaction parameters exert a great influence on the electrochemical performances of the composite, in order to get a higher specific capacitance, the effect of raw graphite material sizes and feeding ratios on the electrochemical properties of such composites have been systematically investigated (Wang et al., 2010b). Specifically, The GO/PANI composite was prepared by an in situ polymerization using a mild oxidant. The composites are synthesized under different mass ratios, using graphite as start material with two sizes: 12 500 and 500 mesh. The result shows that the morphology of the prepared composites is influenced dramatically by the different mass ratios. The highest initial specific capacitances of  $746 \text{ F g}^{-1}$  (12 500 mesh) and  $627 \text{ F g}^{-1}$  (500 mesh) corresponding to the mass ratios 1:200 and 1: 50 (GO/aniline) are obtained, compared to PANI of  $216 \text{ F g}^{-1}$  at  $200 \text{ mA g}^{-1}$  by charge-discharge analysis between 0.0 and 0.4 V. The improved capacitance retention of 73 % (12 500 mesh) and 64 % (500 mesh) after 500 cycles is obtained for the mass ratios 1:23 and 1:19 compared to PANI of 20%. The enhanced specific capacitance and cycling life implies a synergistic effect between two components.

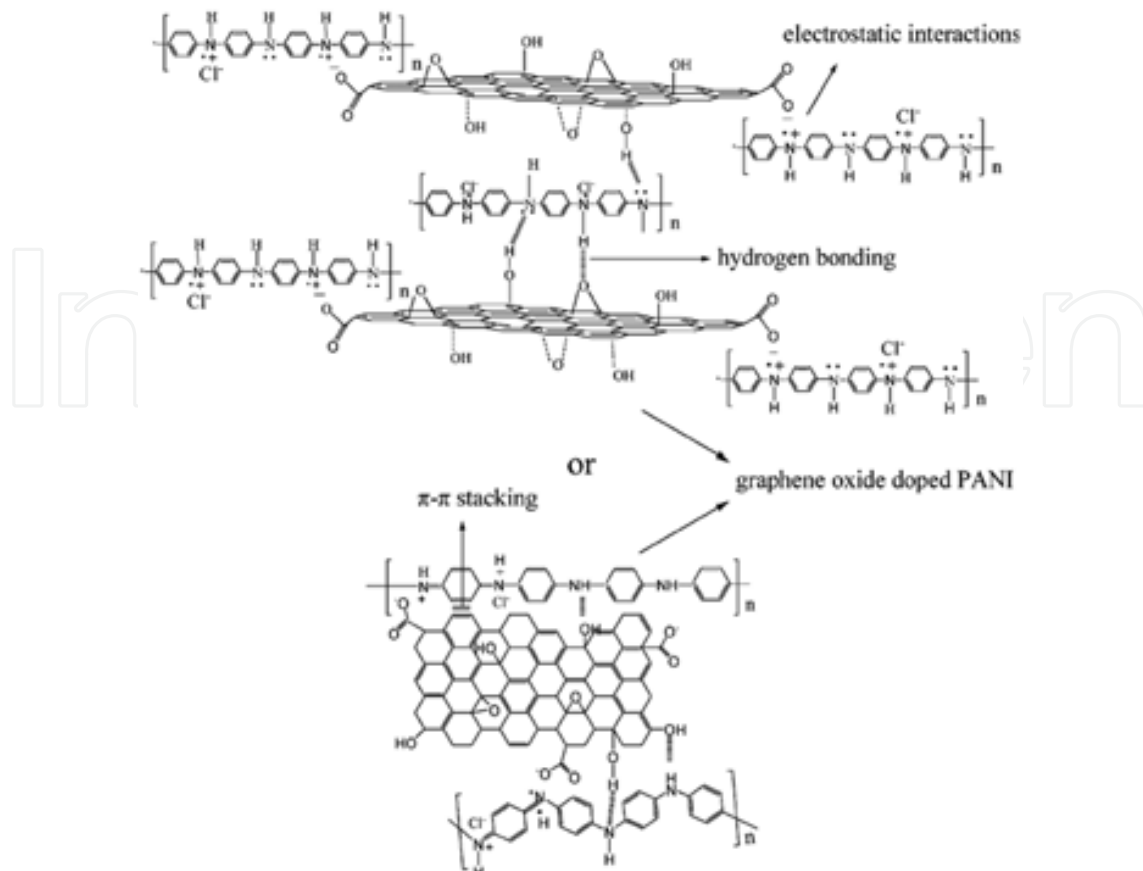


Fig. 21. Proposed possible combining mode of GO/PANI Composite (Wang et al., 2010b).

To prepare graphene-PANI composites, a simple three-step synthesis method was presented by an in situ polymerization-reduction/dedoping-redoping process (Wang et al., 2010c). This method greatly improves the specific capacitance, retention time, energy density, and power density of the composite as electrode material for supercapacitors.

The formation process of the GEP composite is depicted in Fig. 22. The multilayer GO is extensively exfoliated into GEO nanosheets with abundant oxygen containing groups on both face and edges under ultrasonication in ethylene glycol. Such GEO nanosheets facilitate the uniform adsorption of aniline molecules under stirring. When APS and hydrochloric acid are added into the suspension under ice bath, the aniline molecules absorbed on the sheets are initiated to polymerize just from the absorbed sites on the surface, and then the structure of PANI covering nano-sheet slowly forms. This structure of the hybrid material maintains unaltered when GEO sheets are reduced and PANI are dedoped by sodium hydroxide at the temperature of 90 °C for 5 h, and it keeps steady even when PANI nanoparticles are redoped in hydrochloric acid solution. In addition, the morphology of the prepared hybrid material is quite uniform and no individual graphene or PANI agglomerates can be observed, suggesting that graphene sheets are covered by nanostructured PANI granules completely and successfully. It is noteworthy that the hybrid nanosheets can be convoluted freely without being splitting into pieces (Fig. 22, see blue lines in GEOP-1 and GEP-3 in the TEM images), further indicating the flexibility of the composites. The perfect coverage of PANI on graphene makes full use of the large specific area of graphene and could be favorable for the enhancement of electrochemical properties of the composite materials.

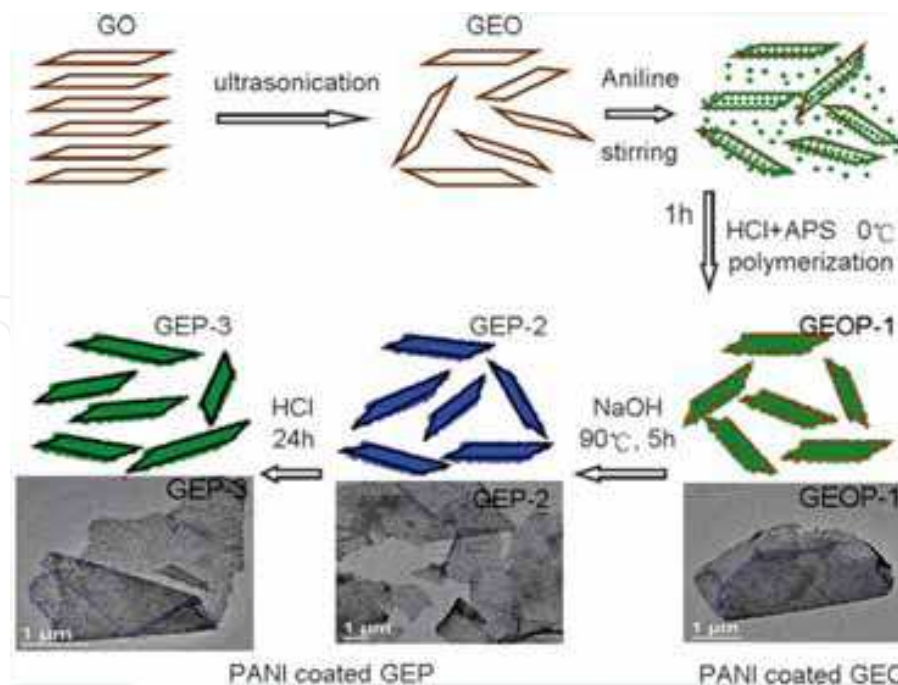


Fig. 22. A scheme illustrating the preparation process of GEP hybrid materials (Wang et al., 2010c).

The electrochemical performance of the electrode materials was analyzed using CV and galvanostatic charge-discharge. Fig. 23a shows the CV curves of the pristine graphene, PANI, GEOP-1, GEP-2 and GEP-3 at a scan rate of  $1 \text{ mV s}^{-1}$  in  $1 \text{ M H}_2\text{SO}_4$  electrolyte in the potential range from  $-0.2$  to  $0.6 \text{ V}$ . Both PANI and the composite electrodes show a pair of redox peaks. The peak positions of individual components are very close to each other and nearly merge into one peak. The specific capacitance was calculated. The pristine graphene electrode exhibits an approximated rectangular shape that is characteristic of an electric double layer capacitance (EDLC) with a specific capacitance of  $316 \text{ F g}^{-1}$ . The PANI electrode shows a pair of redox peak that is characteristic of pseudo-capacitance with the specific capacitance  $777 \text{ F g}^{-1}$ . On the other hand, the CV curves of GEOP-1, GEP-2 and GEP-3 electrodes show a behavior of a combination of both EDLC and redox capacitance with the specific capacitance of  $827$ ,  $1126$  and  $1079 \text{ F g}^{-1}$ , respectively. The specific capacitance changes with different samples were illustrated in Fig. 23b. The GEOP-1 electrode exhibits a sharply increased electrochemical capacitance compared to the graphene electrode. After treating with sodium hydroxide, the specific capacitance of GEP-2 electrode goes as high as  $1126 \text{ F g}^{-1}$ . Although the redoping process leads to a little decrease of the capacitance, the specific capacitance of  $1079 \text{ F g}^{-1}$  for GEP-3 is still higher than GEOP-1 and much better than each component of the hybrid material.

The cycling performance is shown in Fig. 23c and d. Fig. 23c gives a non-linear galvanostatic charge-discharge curve of GEP-2 for the first 1–5 cycles, which presents an evident pseudo-capacitance character. After 1000 cycles the bending extent of the curve becomes weak and the curve tends to linear, but still non-linear. This indicates the contribution of pseudo-capacitance in GEP hybrid materials decreases, and the EDLC effect becomes evident. The CV curves before charge-discharge test and after 1000 cycles are shown in Fig. 23d (inset). A large and wide area of the CV curve with a pair of evident redox peaks can be seen before charge-discharge test, indicating both EDLC and pseudo-capacitance performance of the

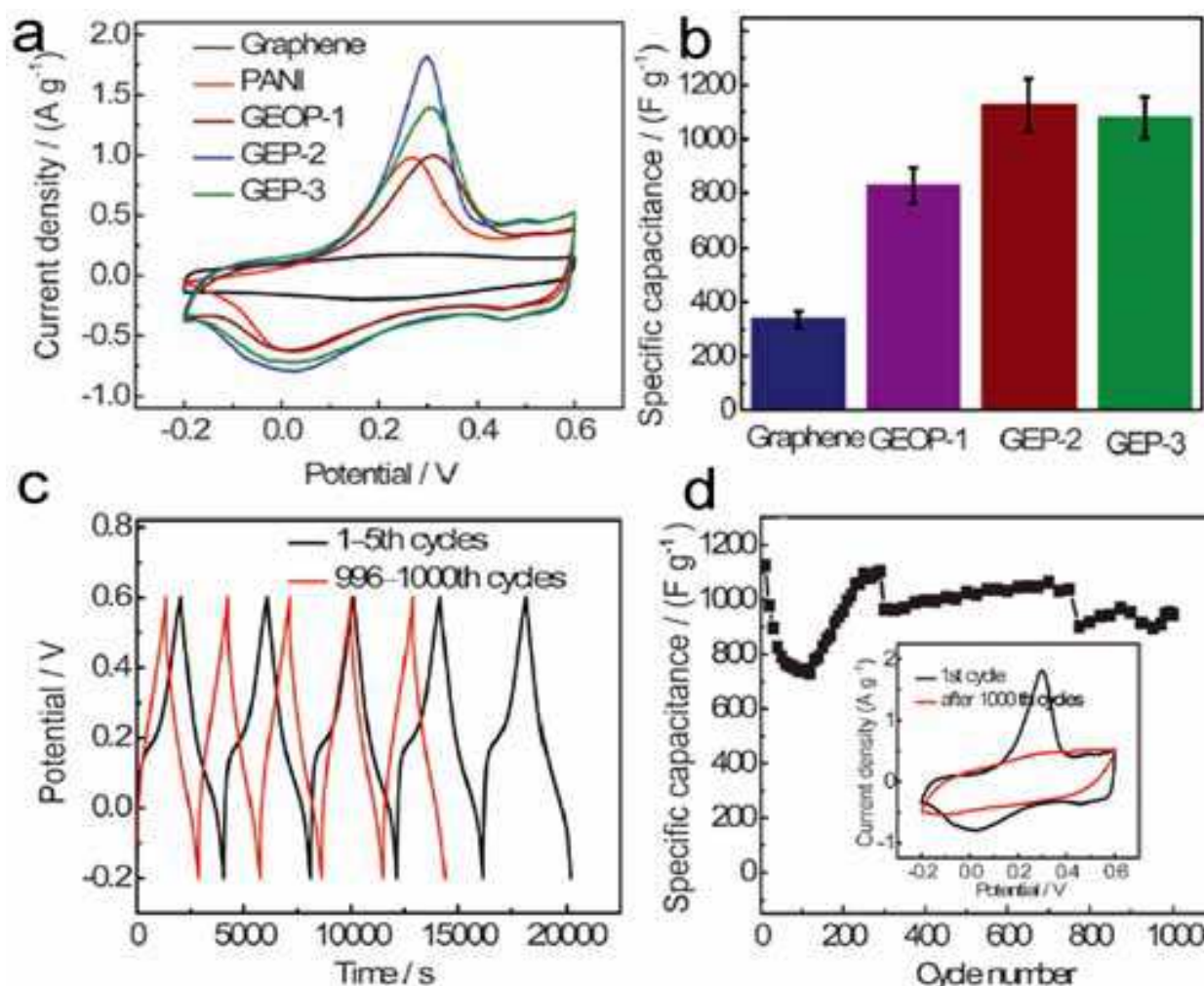


Fig. 23. (a) CV curves of graphene, PANI, GEOP-1, GEP-2 and GEP-3 at  $1 \text{ mV s}^{-1}$  in  $1 \text{ M H}_2\text{SO}_4$  in the potential range from  $-0.2$  to  $0.6 \text{ V}$ ; (b) specific capacitance changes with different samples; (c) comparison of galvanostatic charge-discharge curves of GEP-2 between 1-5th and 996-1000th cycles at  $200 \text{ mA g}^{-1}$  in  $1 \text{ M H}_2\text{SO}_4$  in the potential range from  $-0.2$  to  $0.6 \text{ V}$ ; (d) specific capacitance as a function of cycle number. (Inset: comparison of the CV curves before charge-discharge test and after 1000 cycles for charge-discharge test) (Wang et al., 2010c).

electrode. After 1000th cycles, the redox peaks become weak and nearly disappear. This results from the reduced pseudo-capacitance of PANI. The specific capacitance as a function of cycle number is shown in Fig. 23d. It is interesting that the specific capacitance sharply decreases first for the 1-100 cycles and increases rapidly for 100-200 cycles and then maintain approximately steady after 200 cycles around  $900 \text{ F g}^{-1}$ . The specific capacitance for GEP-2 after 1000 cycles still maintains  $946 \text{ F g}^{-1}$ , corresponding to 84% of the initial cycle. This result is better than that reported for the composites of graphene and PANI with capacitance retention of 84% after only 40 cycles; when the capacitance retention of GEOP-1 after 1000 cycles is 59%. The enhanced retention life for GEP-2 is mainly due to the change from GEO to graphene in the hybrid material, leading to the improvement of mechanical properties of the composite.

## 2.7 Other potential applications

The integration of graphene with other materials has also exhibited additional peculiar properties. For example, a composite of graphene-cuprous oxide has found to be an anode material in lithium ion batteries, giving a high capacity of ca.1100 mAh g<sup>-1</sup> in the first charge-discharge cycle (Xu et al., 2009); the graphene-CdS quantum dot nanocomposite has shown promising optoelectronic performance and may be a potential material in novel semiconductor hybrid system (Cao et al.). Moreover, single-layer graphene can be modulated with various aromatic molecules to be an n- and p-doped type for tailoring its transistor devices (X.Dong et al., 2009); metal particles (Au, Au-Pt alloy, etc.) decorated graphene nanosheets can be used as immobilization matrix for amperometric glucose biosensor (Baby et al., 2010). In addition, Kuc et al. pointed out that the composite of fullerene intercalated graphene sheets has promising applications in hydrogen sieving and storage (Kuc et al., 2006).

## 3. Conclusion and perspectives

During the past few years, significant efforts have been directed toward the preparation of graphene-based nanocomposites, and the highly unique properties of these materials have been demonstrated for a variety of catalysts, supercapacitors and fuel cell batteries. It is indubitable that utilizing graphene-based nanocomposites in either of these technologies is a new endeavor, indicating that future research efforts will be abundant. One of the future challenges is to maintain the excellent physical properties of graphene in the process for synthesizing nanocomposites. It should be pointed out that GO sheets are indisputably effective precursors for bulk production of hybrid materials currently and the major shortcoming of this approach is the loss of conductivity. A seemingly obvious prediction is that a more straightforward route can be developed *via* direct oxidation of pristine graphene in soft manners, so that relatively low amount of functional groups is produced as the anchor sites to decorate graphene with nanoparticles. One feature of such process is that there is no need to reduce the composites because of the low oxidation degree, leading to lower defected frameworks of graphene. Notable is the progress in the area of graphene-based nanocomposites and hybrids. However, much more remains to be done, especially when considering the practical application of these materials in catalysts and electrochemical devices. The opportunities and challenges that rest on these targets should attract the efforts of many scientists and engineers in this important and fantastic field.

## 4. References

- Allen, M. J., Tung, V. C. & Kaner, R. B. (2010). Honeycomb Carbon: A Review of Graphene. *Chem. Rev.*, 110, 1, (Feb-2010), page numbers (132-145), 0009-2665
- Baby, T. T., Aravind, S. S. J., Arockiadoss, T., Rakhi, R. B. & Ramaprabhu, S. (2010). Metal Decorated Graphene Nanosheets as Immobilization Matrix for Amperometric Glucose Biosensor. *Sensors Actuat. B-Chem.*, 145, 1, (Mar-2010), page numbers (71-77), 0925-4005
- Boldyrev, V. V. (2006). Thermal Decomposition of Ammonium Perchlorate. *Thermochim. Acta*, 443, 1, (Apr -2006), page numbers (1-36), 0040-6031

- Bong, S., Kim, Y.-R., Kim, I., Woo, S., Uhm, S., Lee, J. & Kim, H. (2010). Graphene Supported Electrocatalysts for Methanol Oxidation. *Electrochem. Commun.*, 12, 1, (Nov-2010), page numbers (129-131), 1388-2481
- Boukhvalov, D. W. & Katsnelson, M. I. (2008). Modeling of Graphite Oxide. *J Am. Chem. Soc.*, 130, 32, (Jul-2008), page numbers (10697-10701), 0002-7863
- Cao, A., Liu, Z., Chu, S., Wu, M., Ye, Z., Cai, Z., Chang, Y., Wang, S., Gong, Q. & Liu, Y. (2010). A Facile One-step Method to Produce Graphene-CdS Quantum Dot Nanocomposites as Promising Optoelectronic Materials. *Adv. Mater.*, 22, 1, (Jan-2010), page numbers (103-106), 1521-4095
- Chen, S., Zhu, J., Huang, H., Zeng, G., Nie, F. & Wang, X. (2010a). Facile Solvothermal Synthesis of Graphene-MnOOH Nanocomposites. *J Solid State Chem.*, In Press, DOI: 10.1016/j.jssc.2010.08.026, 0022-4596
- Chen, S., Zhu, J. & Wang, X. (2010b). One-Step Synthesis of Graphene-Cobalt Hydroxide Nanocomposites and Their Electrochemical Properties. *J Phys. Chem. C*, 114, 27, (Jun-2010b), page numbers (11829-11834), 1932-7447
- Chen, S., Zhu, J. & Wang, X. (2010c). From Graphene to Metal Oxide Nanolamellas: A Phenomenon of Morphology Transmission. *ACS Nano*, In Press, DOI: 10.1021/nm101857y, 1936-0851
- Chen, S., Zhu, J., Wu, X., Han, Q. & Wang, X. (2010d). Graphene Oxide-MnO<sub>2</sub> Nanocomposites for Supercapacitors. *ACS Nano*, 4, 5, (Apr-2010d), page numbers (2822-2830), 1936-0851
- Devaraj, S. & Munichandraiah, N. (2008). Effect of Crystallographic Structure of MnO<sub>2</sub> on Its Electrochemical Capacitance Properties. *J Phys. Chem. C*, 112, 11, (Feb-2008), page numbers (4406-4417), 1932-7447
- Dikin, D. A., Stankovich, S., Zimney, E. J., Piner, R. D., Dommett, G. H. B., Evmenenko, G., Nguyen, S. T. & Ruoff, R. S. (2007). Preparation and Characterization of Graphene Oxide Paper. *Nature*, 448, 7152, (Jul-2007), page numbers (457-460), 0028-0836
- Ferrari, A. C. (2007). Raman Spectroscopy of Graphene and Graphite: Disorder, Electron-phonon Coupling, Doping and Nonadiabatic Effects. *Solid State Commun.*, 143, 1-2, (Jul-2007), page numbers (47-57), 0038-1098
- Fu, X., Bei, F., Wang, X., O'Brien, S. & Lombardi, J. R. (2010a). Excitation Profile of Surface-Enhanced Raman Scattering in Graphene-Metal Nanoparticle Based Derivatives. *Nanoscale*, 2, 8, (Jun-2010a), page numbers (1461-1466), 2040-3364
- Fu, X., Bei, F., Wang, X., Yang, X. & Lu, L. (2010b). Surface-Enhanced Raman Scattering of Silylated Graphite Oxide Sheets Sandwiched between Colloidal Silver Nanoparticles and Silver Piece. *J Raman Spectrosc.*, 41, 4, (Apr-2010b), page numbers (370-373), 1097-4555
- Geim, A. K. & Novoselov, K. S. (2007). The Rise of Graphene. *Nat. Mater.*, 6, 3, (Mar-2007), page numbers (183-191), 1476-1122
- Hernandez, Y., Nicolosi, V., Lotya, M., Blighe, F. M., Sun, Z., De, S., McGovern, I. T., Holland, B., Byrne, M., Gun'Ko, Y. K., Boland, J. J., Niraj, P., Duesberg, G., Krishnamurthy, S., Goodhue, R., Hutchison, J., Scardaci, V., Ferrari, A. C. & Coleman, J. N. (2008). High-Yield Production of Graphene by Liquid-Phase

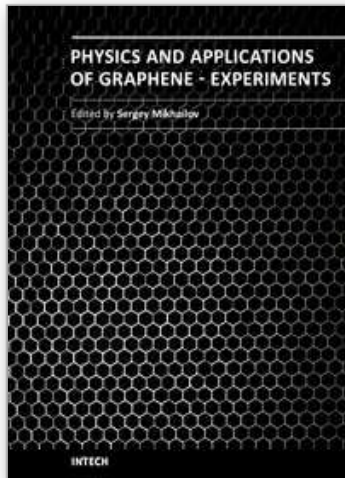
- Exfoliation of Graphite. *Nat. Nanotechnol.*, 3, 9, (Sep-2008), page numbers (563-568), 1748-3387
- Kuc, A., Zhechkov, L., Patchkovskii, S., Seifert, G. & Heine, T. (2006). Hydrogen Sieving and Storage in Fullerene Intercalated Graphite. *Nano Lett.*, 7, 1, (Jan-2006), page numbers (1-5), 1530-6984
- Li, D., Muller, M. B., Gilje, S., Kaner, R. B. & Wallace, G. G. (2008). Processable Aqueous Dispersions of Graphene Nanosheets. *Nat. Nanotechnol.*, 3, 2, (Jan-2008), page numbers (101-105), 1748-3387
- Li, X., Cai, W., An, J., Kim, S., Nah, J., Yang, D., Piner, R., Velamakanni, A., Jung, I., Tutuc, E., Banerjee, S. K., Colombo, L. & Ruoff, R. S. (2009). Large-Area Synthesis of High-Quality and Uniform Graphene Films on Copper Foils. *Science*, 324, 5932, (May-2009), page numbers (1312-1314), 0036-8075
- Lo'pez, V., Sundaram, R. S., Go'mez-Navarro, C., Burghard, D. O. M., Go'mez-Herrero, J., Zamora, F. I. & Kern, K. (2010). Chemical Vapor Deposition Repair of Graphene Oxide: A Route to Highly Conductive Graphene Monolayers. *Adv. Mater.*, 21(Aug-2010), page numbers (4683-4686), 1521-4095
- Lotya, M., Hernandez, Y., King, P. J., Smith, R. J., Nicolosi, V., Karlsson, L. S., Blighe, F. M., De, S., Wang, Z., McGovern, I. T., Duesberg, G. S. & Coleman, J. N. (2009). Liquid Phase Production of Graphene by Exfoliation of Graphite in Surfactant/Water Solutions. *J Am. Chem. Soc.*, 131, 10, (Feb-2009), page numbers (3611-3620), 0002-7863
- Lu, T., Zhang, Y., Li, H., Pan, L., Li, Y. & Sun, Z. (2010) Electrochemical behaviors of graphene-ZnO and graphene-SnO<sub>2</sub> composite films for supercapacitors. *Electrochim. Acta* 55, 13, (May-2010), page numbers (4170-4173), 0013-4686
- Novoselov, K. S., Geim, A. K., Morozov, S. V., Jiang, D., Zhang, Y., Dubonos, S. V., Grigorieva, I. V. & Firsov, A. A. (2004). Electric Field Effect in Atomically Thin Carbon Films *Science*, 306, 5696, (Oct-2004), page numbers (666-669), 0036-8075
- Novoselov, K. S., Geim, A. K., Morozov, S. V., Jiang, D., Katsnelson, M. I., Grigorieva, I. V., Dubonos, S. V. & Firsov, A. A. (2005). Two-dimensional Gas of Massless Dirac Fermions in Graphene. *Nature.*, 438, 7065, (Nov-2005), page numbers (197-200), 0028-0836
- Park, H. J., Meyer, J., Roth, S. & Ska'kalova', V. (2010). Growth and properties of few-layer graphene prepared by chemical vapor deposition. *Carbon*, 48, 4, (Apr-2010), page numbers (1088-1094), 0008-6223
- Park, S. & Ruoff, R. S. (2009). Chemical Methods for the Production of Graphenes. *Nat. Nanotechnol.* 4, (Mar-2009), page numbers (217-224), 1748-3387
- Stankovich, S., Dikin, D. A., Kohlhaas, K. M., Zimney, E. J., Stach, E. A., Piner, R. D., Nguyen, S. T. & Ruoff, R. S. (2006). Graphene-Based Composite Materials. *Nature* 442, 7100, (Jul-2006), page numbers (282-286), 0028-0836
- Stoller, M. D., Park, S., Zhu, Y., An, J. & Ruoff, R. S. (2008). Graphene-Based Ultracapacitors. *Nano Lett.* 8, 10, (Sep-2008), page numbers (3498-3502), 1530-6984
- Wang, B., Park, J., Wang, C., Ahn, H. & Wang, G. Mn<sub>3</sub>O<sub>4</sub> Nanoparticles Embedded Mn<sub>3</sub>O<sub>4</sub> into Graphene Nanosheets: Preparation, Characterization, and Electrochemical

- Properties for Supercapacitors. *Electrochim. Acta*, 55, 22, (Sep-2010), page numbers (6812-6817), 0013-4686
- Wang, H., Hao, Q., Yang, X., Lu, L. & Wang, X. (2009a). Graphene Oxide Doped Polyaniline for Supercapacitors. *Electrochem. Commun.*, 11, 6, (Jun-2009a), page numbers (1158-1161), 1388-2481
- Wang, H., Casalongue, H. S., Liang, Y. & Dai, H. (2010a). Ni(OH)<sub>2</sub> Nanoplates Grown on Graphene as Advanced Electrochemical Pseudocapacitor Materials. *J Am. Chem. Soc.*, 132, 21, (May-2010a), page numbers (7472-7477), 0002-7863
- Wang, H., Hao, Q., Yang, X., Lu, L. & Wang, X. (2010b). Effect of Graphene Oxide on the Properties of Its Composite with Polyaniline. *ACS Applied Mater. Interf.* 2, 3, (Mar-2010b), page numbers (821-828), 1944-8244
- Wang, H., Hao, Q., Yang, X., Lu, L. & Wang, X. (2010c). A Nanostructured Graphene/Polyaniline Hybrid Material for Supercapacitors. *Nanoscale*, In Press, DOI: 10.1039/C0NR00224K, 2040-3364
- Wang, Y., Shi, Z., Huang, Y., Ma, Y., Wang, C., Chen, M. & Chen, Y. (2009b). Supercapacitor Devices Based on Graphene Materials. *J Phys. Chem. C*, 113, 30, (Jul-2009b), page numbers (13103-13107), 1932-7447
- Weixia, Z., Jiecheng, C., Cheng-an, T., Yiguang, W., Zhanping, L., Li, M., Yuquan, W. & Guangtao, L. (2009). A Strategy for Producing Pure Single-Layer Graphene Sheets Based on a Confined Self-Assembly Approach. *Angew. Chem. Int. Ed.*, 48, 32, (Jul-2009), page numbers (5864-5868), 1521-3773
- Williams, G., Seger, B. & Kamat, P. V. (2008). TiO<sub>2</sub>-Graphene Nanocomposites. UV-Assisted Photocatalytic Reduction of Graphene Oxide. *ACS Nano* 2, 7, (Jul-2008), page numbers (1487-1491),
- Wu, C., GuofaDong & LunhuiGuan. (2010). Production of Graphene Sheets by a Simple Heliumarc-Discharge. *Physica E: Low-Dimensional Systems and Nanostructures* 42, 5, (Mar-2010), page numbers (1267-1271), 1386-9477
- X.Dong, D., Dongliang, F., Wenjing, F., Yumeng, S., Peng, C. & Lain-Jong, L. (2009). Doping Single-Layer Graphene with Aromatic Molecules. *Small* 5, 12, (Jun-2009), page numbers (1422-1426), 1613-6829
- Xu, C., Wang, X. & Zhu, J. (2008a). Graphene & Metal Particle Nanocomposites. *J Phys. Chem. C* 112, 50, (Nov-2008a), page numbers (19841-19845), 1932-7447
- Xu, C., Wang, X., Zhu, J., Yang, X. & Lu, L. (2008b). Deposition of Co<sub>3</sub>O<sub>4</sub> nanoparticles onto exfoliated graphite oxide sheets. *J Mater. Chem.*, 18, 46, (Sep-2008b), page numbers (5625-5629), 0959-9428
- Xu, C. & Wang, X. (2009). Fabrication of Flexible Metal-Nanoparticle Films Using Graphene Oxide Sheets as Substrates. *Small*, 5, 19, (Aug-2009), page numbers (2212-2217), 1613-6829
- Xu, C., Wang, X., Yang, L. & Wu, Y. (2009). Fabrication of a Graphene-Cuprous Oxide Composite. *J Solid State Chem.*, 182, 9, (Sep-2009), page numbers (2486-2490), 0022-4596
- Yan, J., Fan, Z., Wei, T., Qian, W., Zhang, M. & Wei, F. (2010). Fast and Reversible Surface Redox Reaction of Graphene-MnO<sub>2</sub> Composites as Supercapacitor Electrodes. *Carbon* 48, 13, (Nov-2010), page numbers (3825-3833), 0008-6223

- Zhang, Y., Tan, Y.-W., Stormer, H. L. & Kim, P. (2005). Experimental Observation of the Quantum Hall Effect and Berry's Phase in Graphene. *Nature* 438, 7065, (Nov-2005), page numbers (201-204),
- Zhu, J., Zeng, G., Nie, F., Xu, X., Chen, S., Han, Q. & Wang, X. (2010). Decorating Graphene Oxide with CuO Nanoparticles in a Water-isopropanol System. *Nanoscale*, 2(Apr-2010), page numbers (988-994), 2040-3364

IntechOpen

IntechOpen



## **Physics and Applications of Graphene - Experiments**

Edited by Dr. Sergey Mikhailov

ISBN 978-953-307-217-3

Hard cover, 540 pages

**Publisher** InTech

**Published online** 19, April, 2011

**Published in print edition** April, 2011

The Stone Age, the Bronze Age, the Iron Age... Every global epoch in the history of the mankind is characterized by materials used in it. In 2004 a new era in material science was opened: the era of graphene or, more generally, of two-dimensional materials. Graphene is the strongest and the most stretchable known material, it has the record thermal conductivity and the very high mobility of charge carriers. It demonstrates many interesting fundamental physical effects and promises a lot of applications, among which are conductive ink, terahertz transistors, ultrafast photodetectors and bendable touch screens. In 2010 Andre Geim and Konstantin Novoselov were awarded the Nobel Prize in Physics "for groundbreaking experiments regarding the two-dimensional material graphene". The two volumes *Physics and Applications of Graphene - Experiments* and *Physics and Applications of Graphene - Theory* contain a collection of research articles reporting on different aspects of experimental and theoretical studies of this new material.

### **How to reference**

In order to correctly reference this scholarly work, feel free to copy and paste the following:

Xin Wang and Sheng Chen (2011). Graphene-Based Nanocomposites, *Physics and Applications of Graphene - Experiments*, Dr. Sergey Mikhailov (Ed.), ISBN: 978-953-307-217-3, InTech, Available from: <http://www.intechopen.com/books/physics-and-applications-of-graphene-experiments/graphene-based-nanocomposites>

**INTECH**  
open science | open minds

### **InTech Europe**

University Campus STeP Ri  
Slavka Krautzeka 83/A  
51000 Rijeka, Croatia  
Phone: +385 (51) 770 447  
Fax: +385 (51) 686 166  
[www.intechopen.com](http://www.intechopen.com)

### **InTech China**

Unit 405, Office Block, Hotel Equatorial Shanghai  
No.65, Yan An Road (West), Shanghai, 200040, China  
中国上海市延安西路65号上海国际贵都大饭店办公楼405单元  
Phone: +86-21-62489820  
Fax: +86-21-62489821

© 2011 The Author(s). Licensee IntechOpen. This chapter is distributed under the terms of the [Creative Commons Attribution-NonCommercial-ShareAlike-3.0 License](#), which permits use, distribution and reproduction for non-commercial purposes, provided the original is properly cited and derivative works building on this content are distributed under the same license.

IntechOpen

IntechOpen